Materials Today • Volume 42 • January/February 2021 **RESEARCH**

Understanding all solid-state lithium batteries through *in situ* transmission electron microscopy

Yong Cheng [1,†], Liqiang Zhang [2,†], Qiaobao Zhang [1,*], Jie Li [5], Yongfu Tang [2], Claude Delmas [6], Ting Zhu [4], Martin Winter [5], Ming-Sheng Wang [1,*], Jianyu Huang [2,3,*]

[1] Department of Materials Science and Engineering, College of Materials, Xiamen University, Xiamen, Fujian 361005, PR China
[2] Clean Nano Energy Center, State Key Laboratory of Metastable Materials Science and Technology, Yanshan University, Qinhuangdao 066004, PR China
[3] School of Materials Science and Engineering, Xiangtan University, Xiangtan, Hunan 411105, PR China
[4] Woodruff School of Mechanical Engineering, Georgia Institute of Technology, Atlanta, GA 30332, United States
[5] Helmholtz-Institute Münster (IEK-12), Forschungszentrum Jülich GmbH, Corrensstraße 46, 48149, Münster, Germany
[6] CNRS, Univ. Bordeaux, Bordeaux INP, ICMCB UMR 5026, F 33600 Pessac, France

Owing to the use of solid electrolytes instead of flammable and potentially toxic organic liquid electrolytes, all solid-state lithium batteries (ASSLBs) are considered to have substantial advantages over conventional liquid electrolyte based lithium ion batteries (LIBs) in terms of safety, energy density, battery packaging, and operable temperature range. However, the electrochemistry and the operation mechanism of ASSLBs differ considerably from conventional LIBs. Consequently, the failure mechanisms of ASSLBs, which are not well understood, require particular attention. To improve the performance and realize practical applications of ASSLBs, it is crucial to unravel the dynamic evolution of electrodes, solid electrolytes, and their interfaces and interphases during cycling of ASSLBs. *In situ* transmission electron microscopy (TEM) provides a powerful approach for the fundamental investigation of structural and chemical changes during operation of ASSLBs with high spatio-temporal resolution. Herein, recent progress in *in situ* TEM studies of ASSLBs are reviewed with a specific focus on real-time observations of reaction and degradation occurring in electrodes, solid electrolytes, and their interfaces. Novel electro-chemo-mechanical coupling phenomena are revealed and mechanistic insights are highlighted. This review covers a broad range of electrode and electrolyte materials applied in ASSLBs, demonstrates the general applicability of *in situ* TEM for elucidating the fundamental mechanisms and providing the design guidance for the development of high-performance ASSLBs. Finally, challenges and opportunities for *in situ* TEM studies of ASSLBs are discussed.

Keywords: *In situ* transmission electron microscopy; All solid-state lithium batteries; Electrodes; Interfaces; Reaction mechanism.

Introduction

With an ever-increasing demand for clean and renewable energy, energy storage technologies with high energy or power density have attracted significant attention in recent years [1,2]. Lithium ion batteries (LIBs) have been widely adopted in portable electronics and electric vehicles, primarily due to their high operating voltage, high energy density, and lack of memory effect [3–8]. Still existing safety concerns on LIBs are largely originated from the employment of organic carbonate electrolytes, which

---

* Corresponding authors.
E-mail addresses: Zhang, Q. (zhangqiaobao@xmu.edu.cn), Wang, M.-S. (mswang@xmu.edu.cn), Huang, J. (jhuang@ysu.edu.cn).

† These authors contributed equally to this work.

1369-7021/ https://doi.org/10.1016/j.mattod.2020.09.003

tend to decompose at high operation voltage and react with electrode materials during charge and discharge, resulting in an irreversible loss of battery cell capacity [9,10]. Additionally, liquid electrolytes are prone to leak, evaporate, ignite, and sometimes even explode in a practical battery cell. Furthermore, the extremely high reactivity of liquid organic electrolytes with metallic lithium (Li) in rechargeable Li metal batteries causes safety concerns such as fire hazard [11-13]. To tackle these challenges, significant efforts have been devoted to develop Li batteries that are safer, and at the same time show hopefully even better performance than LIBs. In recent years, several solid electrolytes have been widely recognized as potential solutions to mitigate the aforementioned problems of liquid electrolytes in LIBs and Li metal batteries [14]. Hence, Li batteries with solid electrolytes, called all solid-state Li batteries (ASSLBs), are believed to be among the most promising candidates for next generation rechargeable batteries [15–19].

While ASSLBs provide certain advantages over conventional LIBs with liquid electrolyte, great challenges remain to realize their practical application as energy storage systems in electric vehicles and grid storage. Issues regarding electrode materials and electrolytes as well as their interfaces, have to be tackled urgently [20–23]. Problems originating from the highly complex dynamic evolution of electrodes, electrolytes and interphases, *i.e.* solid electrolyte interphase (SEI) and cathode electrolyte interphase (CEI) during battery cell operation are difficult to investigate in sealed ASSLIB cells under realistic operation conditions. For example, several potential high-capacity electrode materials in ASSLBs suffer from drastic chemical and structural changes during cycling, resulting in electrochemical and mechanical degradation processes that are not well understood to date. Nanomaterials are promising candidates for electrode materials in ASSLBs, because their small feature sizes enable fast Li ion transport, giving high rate performance. However, the mechanisms of ion and electron transport in nanomaterials have not been well understood. In addition, little is known for the interfaces between electrodes containing nanomaterials and electrolytes, including formation, evolution and degradation mechanisms. To design ASSLBs with long life and high efficiency, it is essential to gain a deep understanding of the electrochemical behavior of electrodes, solid electrolyte materials and their interfaces. Particularly, it is important to elucidate the mechanism of Li dendrite growth, the origin of increasing impedance, and the dynamic process of chemical and structural degradation of the solid electrodes and electrolyte materials and their interfaces during cycling, which are roadblocks that severely hinder broad application of ASSLBs.

During the past several decades, a variety of material and electrochemical characterization techniques, including X-ray and neutron scattering, Raman, Fourier transform infrared spectroscopy, cathodoluminescence, and electrochemical impedance spectroscopy, have been widely used to study battery materials [24–27]. However, these techniques are insufficient to fully address the aforementioned challenges in the study of ASSLBs due to their limited spatiotemporal resolution [28]. In 2010, Huang et al. created the first working Li ion cell inside a transmission electron microscope, realizing the real-time, atomic-scale observation of charge and discharge processes of individual SnO_2 nanowires [29]. Since then, *in situ* TEM has been extensively developed to study the electrochemical processes of LIBs [30–44].

In situ TEM setups for battery studies are usually sealed liquid cell or open cell configurations. The liquid cell is used in the researches of liquid electrolyte based batteries, while the open cell plays a vital role in studying solid batteries. The key components for an open cell include a cathode, an anode, and an inorganic solid electrolyte. According to the electrolytes, the open cell of ASSLBs can be further divided into two types. As shown in Fig. 1, the solid-state open cell [45], gaseous environmental open cell [46], and atomic force microscope with environmental transmission electron microscope (AFM-ETEM) open cell [47,48] use the naturally formed lithium oxide, nitride or carbonate (*i.e.* Li_2O, LiO_xN_y, Li_2CO_3) as the solid electrolyte, which are able to reveal the reaction mechanisms and electro-chemo-mechanical behavior of electrode materials under routine or atmospheric conditions. Another type of open cell for ASSLBs that use the traditional solid electrolyte, including the solid-state nanowire core-multi-shell cell [49], solid-state thin film cell [50], and solid polymer electrolyte open cell [51], which principally focus on the structure evolutions of solid electrolytes and the interface behaviors between electrolytes and electrodes. As summarized in Fig. 1, using these open cells and in combination with various imaging and analytical techniques of TEM [52], the morphological evolution, reaction kinetics, phase transformations, chemical changes, mechanical stress, SEI and CEI formation, electric potential distribution, interfacial behavior, and others in ASSLBs can be obtained by *in situ* TEM. In particular, the new understanding and insights obtained via *in situ* TEM studies are often unique and cannot be obtainable by conventional experimental techniques. Hence, *in situ* TEM creates opportunities of addressing some of the long-standing problems in the field of ASSLBs [53–55].

It should also be pointed out that the solid electrolytes are very important in ASSLBs, but the changes in electrode materials are also very important. Choosing Li_2O as an electrolyte is a little different from a real battery, but this method is simple to realize in the TEM, and Li_2O is only used as a channel for Li^+ transmission, so it does not affect the experimental results. Moreover, it is generally accepted that the materials behavior observed by *in situ* TEM using the Li_2O as solid electrolyte with the open cell design reflects the real battery electrochemistry in terms of the structural and chemical evolution of electrodes upon lithiation/delithiation [56,57]. In fact, in the past few years, *in situ* TEM studies of LIBs have been carried out based on the open cell and provided important fundamental information about the reaction kinetics and microstructural evolution during battery operations in real time [57,58]. For example, the developed "*operando*" TEM electrochemical liquid cell consisting of the configuration of a real battery with a relevant liquid electrolyte indicates that the structural and chemical evolution of Si nanowires in both the open cell design and closed cell designs being similar except for the formation of a thick SEI layer on the nanowires [56,59]. Liu et al. have reported anisotropic swelling of Si nanowires during lithiation by using the open cell in TEM [45]. Anisotropic lithiation of Si nanopillars and microslabs have been reported by other groups using *ex situ* experiments based on real LIBs [60,61]. The consistency shows that the electrochemical-

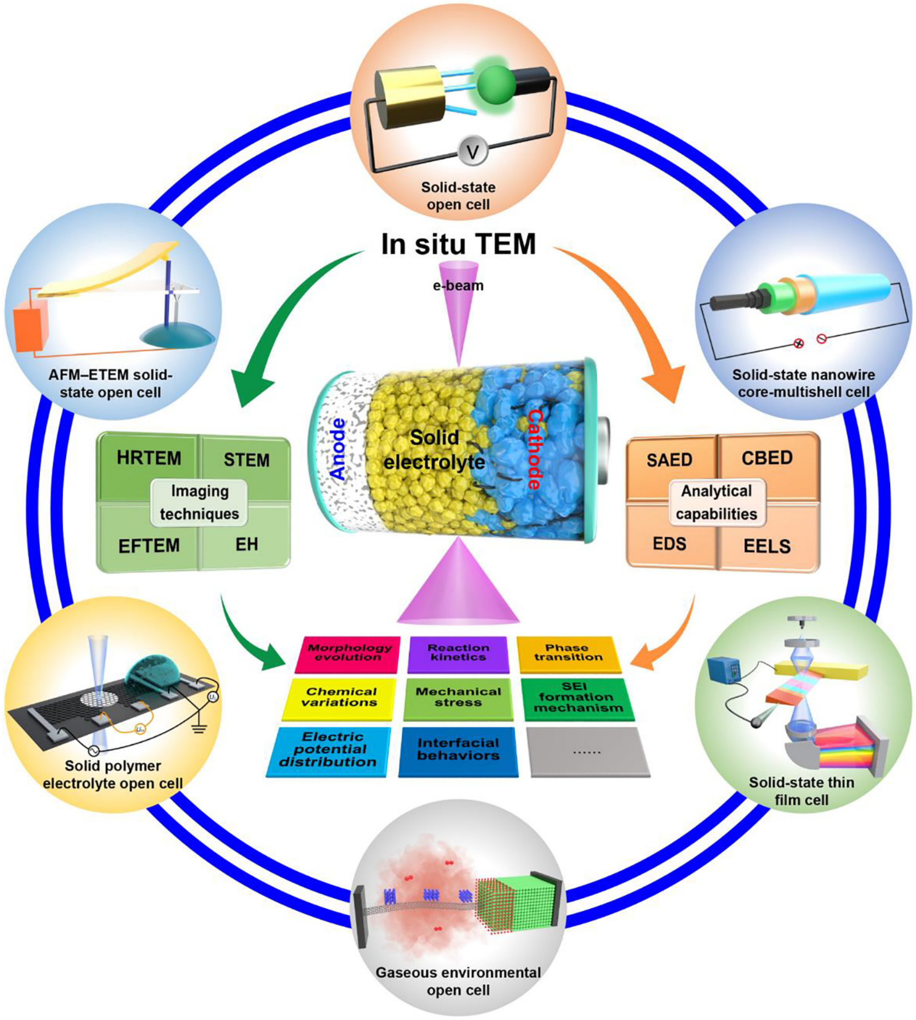

FIGURE 1

Overview of *in situ* TEM techniques and devices in the study of ASSLBs. TEM: transmission electron microscopy; HRTEM: high-resolution TEM; STEM: scanning transmission electron microscopy; SAED: selected area electron diffraction; EDS: energy-dispersive X-ray spectroscopy; CBED: convergent beam electron diffraction; EELS: electron energy loss spectroscopy; HAADF: high-angle annular dark-field; EFTEM: energy-filtered TEM. Reproduced with permission [45–47,49–52].

mechanical response observed in *in situ* TEM is intrinsic to the electrode materials and the information obtained from the *in situ* TEM studies on the dynamic structural and chemical evolution of both the electrode and solid electrolyte materials during lithiation/delithiation is comparable to that of the real ASSLBs.

Given great progress made for understanding interfaces, interphases and materials challenges in ASSLBs via *in situ* TEM, it is an opportune time to review the state-of-the-art research and offer perspectives on future directions in this field. There are several recent review papers on *in situ* TEM studies of battery materials that mainly focus on anode materials applied in conventional LIBs with liquid electrolytes [42,58,62–69]. However, *in situ* TEM studies on Li metal, which is the most desired anode material for high energy density ASSLBs, have not been covered in those review papers. Moreover, cathode materials, solid electrolytes and electrode/electrolyte interfaces as well as related interphases are not sufficiently addressed in those review papers either. Therefore, a comprehensive review of *in situ* TEM studies of ASSLBs, including all components employed, is crucially needed to cover the current status and future directions in this fast-evolving field.

Here we present an overview of recent progress on *in situ* TEM studies for understanding the critical issues in ASSLBs. We highlight novel *in situ* TEM observations for Li metal anodes as well as a variety of cathodes and solid electrolyte/electrode interfaces. Detailed analysis is provided to elucidate the mechanisms of chemical and structural changes in solid electrode and electrolyte materials and their interfaces. Mechanistic insights and design guidance are offered to address the critical challenges in ASSLBs. Last but not the least, we conclude our perspectives of important unresolved issues and future opportunities for the rapidly expanding field of *in situ* TEM for ASSLBs.

In situ TEM studies for cathode materials

The cathode is a critical component that usually determines the energy density and production cost of a battery system. The commonly used cathode materials for ASSLBs are Li transition metal layered oxides (L*TM*O, *TM* = Co, Ni, Mn *etc*.), olivine $LiFePO_4$, spinel $LiMn_2O_4$, *etc.* [70,71]. In addition, sulfur, selenium, metal sulfides and metal fluorides are also promising candidates of cathode materials for ASSLBs due to their high theoretical capacities [72–76], which theoretically can be an order of magnitude higher than that of transition metal oxide cathodes. Furthermore, oxygen cathodes have drawn substantial attention and shown significant potential for applications in future battery technologies [16,77]. *In situ* TEM has played an important role in revealing the working mechanisms of these cathode materials, which is essential to the future development of cathode materials in general.

Li transition metal oxides and polyanionic compounds

The layered $LiCoO_2$ (LCO) developed by Goodenough and Mizushima in the 1980s was the first commercially used cathode material for LIBs [78]. Today, it still dominates the market of portable electronic devices due to its high volumetric density. In the past decade, tremendous effort has been dedicated to understanding the chemical and structural changes of LCO cathodes during electrochemical cycling via both *in situ* and *ex situ* experiments. It has been commonly recognized that LCO cathodes undergo a series of phase transitions from a layered structure to a spinel structure and further to a rock salt structure when operating in conventional liquid electrolytes at high voltage [79–82]. However, the phase transitions of LCO in contact with a solid electrolyte in ASSLBs are not fully understood. To address this issue, Gong et al. constructed an open cell consisting of a LCO cathode, a LLZO solid electrolyte ($Li_{6.75}La_{2.84}Y_{0.16}Zr_{1.75}Ta_{0.25}O_{12}$) and a gold anode, and then performed *in situ* atomic-scale observation of LCO cathodes during delithiation [83]. As shown in Fig. 2a, after high-voltage delithiation, a single crystal LCO became polycrystalline LCO consisting of grains (of approximately 5–15 nm in size) as well as coherent twin boundaries and antiphase domain boundaries. Theoretical calculations indicated that the coherent twin boundary was more likely formed than the antiphase domain boundary during delithiation due to its lower interface energy. The combined *in situ* STEM results and theoretical calculations imply that the nanocrystallization of LCO in ASSLBs could be attributed to the poor physical contact or even only point contact between the electrode and solid electrolyte materials. During the delithiation process, only the contact point/area can transmit Li ions and thus plays the role of seeding the formation of nanograins; the grain boundaries formed in a manner similar to roots growth from seeds, resulting in the monocrystal-polycrystal transition of LCO cathodes that differed from the phase transitions in liquid electrolytes of conventional LIBs. It should be noted that nanocrystallization of LCO was not observed in liquid electrolyte based LIBs, although cracks and dislocations were frequently detected [84]. It is possible that the nanocrystallization observed in the *in situ* nanobattery might be caused by the high voltage applied (5 V) and very short charge time (7 s).

Atomic-scale structural and chemical changes of LCO upon contact with Li dendrites in ASSLBs (*i.e.* overlithiation of LCO) were studied by using *in situ* TEM. Yang et al. reported that spontaneous and fast chemical reactions occurred between the Li metal and the LCO cathode using Li_2O as the solid electrolyte, leading to the expansion and pulverization of LCO and the formation of Li_2O and Co metal [85]. It is worth noting that such chemical reactions were irreversible and independent of the crystallographic orientation of LCO, suggesting that epitaxy measures cannot offer enhanced stability against Li dendrites. Moreover, an intermediate CoO phase was identified at the reaction front, which was induced by a low barrier topotactic phase transition, as shown in Fig. 2b. The emergence of the CoO phase suggests a two-step conversion reaction between Li dendrites and LCO cathode: (1) $Li + LiCoO_2 \rightarrow CoO + Li_2O$; (2) $CoO + 2Li \rightarrow Co + Li_2O$. These results unveiled a failure mechanism of LCO cathodes caused by Li dendrites in ASSLBs.

Ni-rich layered oxides have been also considered as the promising cathodes for ASSLBs due to their high energy density, which approximately proportional to their Ni content. Among them, one of the optimized compositions that emerged is $Li_xNi_{0.8}Co_{0.15}Al_{0.05}O_2$ (NCA), currently in widespread commercial use [86,87]. The majority of studies of NCA have focused on the structural and electrochemical characterization. However, the Li ion diffusion in NCA cathodes remains largely unknown, especially in high-rate reactions. Toward this end, Nomura et al. built a bulk-type ASSLB consisting of the NCA particles coated with 7 nm thick $LiNbO_3$ as the cathode, the indium metal foil as the anode, and the sulfide-based glass–ceramic $75Li_2S\text{-}25P_2S_5$ (LPS) particles as the solid electrolyte in a TEM, and then visualized the dynamics of Li ion using operando STEM-EELS [88]. They found that the Li concentration in most NCA nanocrystals were uniformly distributed, regardless of low-rate and high-rate charge conditions. But the Li concentration had drastic changes at some grain boundaries between the adjacent nanocrystals under high-rate charge conditions (Fig. 2c), indicating that the grain boundaries obstruct the Li ion transportation between the nanocrystals and thus leading to a high resistance in NCA particle cathodes. Through the results of diffraction patterns obtained via four-dimensional STEM, the slow Li ion diffusion at grain boundaries was proved to be due to the crystal orientation mismatch. Therefore, the rate performance of NCA could be improved by optimizing the interfacial structure along with nanocrystal orientation or using large single crystals without boundaries.

$LiMn_2O_4$ spinel and its derivatives are another type of promising cathode materials for ASSLBs due to their facile preparation, abundance of raw materials, low cost and non-toxicity [89–91]. In particular, the spinel $LiNi_{0.5}Mn_{1.5}O_4$ (LNMO) possesses high working potential (4.7 V *vs.* Li/Li^+), and good cycling performance [92,93]. However, LNMO has several drawbacks that must be addressed before their practical applications [94–96], including capacity degradation at high temperature and poor initial Coulombic efficiency, *etc*. Therefore, efforts are needed to understand the structural evolution and underlying mechanisms of LNMO [97,98]. Recently, Gong et al. assembled an open cell consisting of a LNMO cathode, a LLZO solid electrolyte and an gold anode, and then used *in situ* TEM to study the delithiation of the ordered spinel LNMO cathode with phase group of $P4_332$ [99]. The results showed that three different regions, including the transition-metal-rich regions, antiphase boundary regions and transition-metal migration-front regions, formed during delithiation under the <112> zone axis. This was attributed to the uneven extraction of lithium ions and the migration of

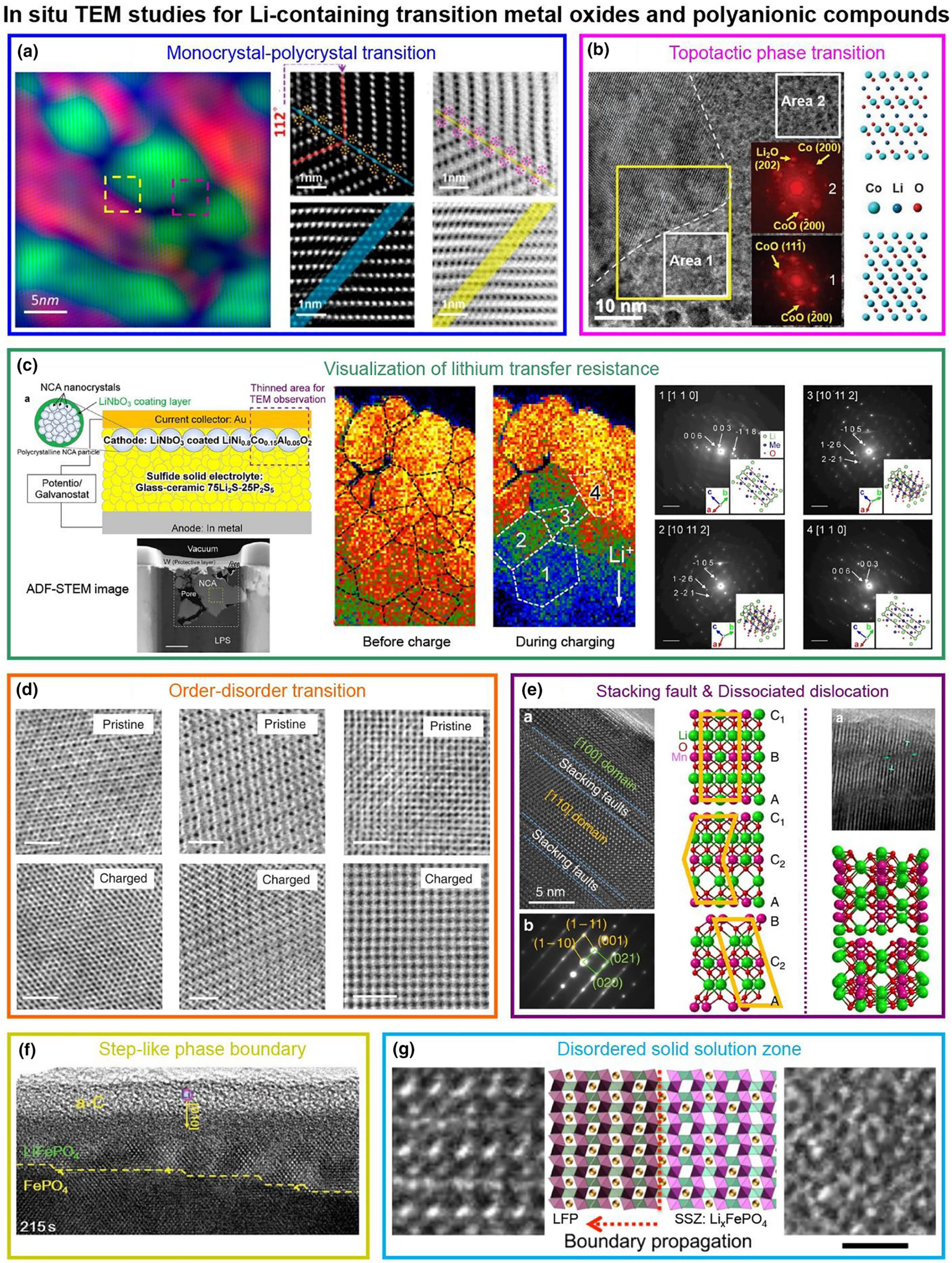

FIGURE 2

In situ TEM studies for Li transition metal oxides and polyanionic compounds. (a) Monocrystal-polycrystal transition along with the formation of antiphase domain boundaries and coherent twin boundaries in LCO cathode during delithiation. Reproduced with permission [83]. (b) Topotactic phase transition from LCO to CoO at the reaction front during lithiation. Reproduced with permission [85]. (c) Visualization of lithium transfer resistance at some grain boundaries between NCA nanocrystals under high-rate reaction conditions, and the relationship between the concentration gradient and crystal orientation. Reproduced with permission [88]. (d) Ordered to disordered structural transition along the <1 0 0>, <1 1 0>, <1 1 1> directions in LNMO during delithiation. Reproduced with permission [99]. (e) Two types of defects (stacking fault and dissociated dislocations) in Li_2MnO_3 during delithiation. Reproduced with permission [113]. (f) Migration of step-like FP/LFP phase boundary in FP during lithiation. Reproduced with permission [120]. (g) Disordered solid solution zone of Li sublattice in LFP during delithiation. Reproduced with permission [121].

transition-metal ions to the 4a (16c in *Fd_3m* space group, disorder LNMO phase) sites of the LNMO cathode. Different from the inhomogeneous transition-metal ion migration along <1 1 2> zone axis, the migration of transition metal ions along the <1 0 0>, <1 1 0> and <1 1 1> zone axes was homogeneous and exhibited an order–disorder transition such that the original Ni/Mn ordered structure became totally disordered, as shown in Fig. 2d. The EELS spectra analysis further indicated that Ni ions were more likely to occupy the 4a sites than Mn ions, and there was a change of valence state in Ni (increase) and Mn (decrease) associated with oxygen loss during delithiation. Based on these *in situ* results, theoretical calculations showed that atomic-scale substitution of Ni and Mn with low valence-state cations could effectively enhance the stability of the LNMO structure. This atomic-scale characterization further provides a deep understanding of the dynamic process and underlying mechanisms of delithiation/lithiation of LNMO materials.

Lithium-rich layered oxide (LRO) cathode materials have also attracted much attention because of their much higher capacity than those of conventional cathodes [100–107]. As the parent component of LRO, Li_2MnO_3 cathode materials have been widely studied, and research has focused on structural changes and oxygen loss during delithiation [108–112]. However, a comprehensive understanding of the complex reaction mechanisms is still lacking, which is critical for overcoming its rapid degradation. To provide in-depth insights into the underlying failure mechanisms in the Li_2MnO_3 cathode, Li et al. investigated the relationship between crystalline defects and Li extraction and oxygen evolution reactions in Li_2MnO_3 using *in situ* TEM (Li_2O was acted as the solid electrolyte) [113]. As shown in Fig. 2e, two types of defects were observed during delithiation of Li_2MnO_3, *i.e.* stacking faults with the fault vector $b/6[110]$ and dissociated dislocations with the Burgers vector of $c/2[0\,0\,1]$. The stacking faults appeared to have low mobility and contributed minimally to oxygen release from the structure. By contrast, due to their high glide mobility, dissociated dislocations caused the formation of oxygen related species, and assisted the transport of oxygen related species to the electrode surfaces, thereby leading to the irreversible formation and release of O_2 gas. This study reveals the role of crystalline defects in the electrochemical behavior of Li_2MnO_3 cathode materials.

Among conventional cathodes, the olivine-type $LiFePO_4$ (LFP) has received great attention as a highly competitive cathode material because of its excellent cycling rate performance, environmental inertness, and low cost [114,115]. It undergoes two phase reaction during cycling, which is formally expressed as $LiFePO_4 - xLi^+ - xe^- \rightarrow xFePO_4 + (1-x)\ LiFePO_4$ (charge) and $FePO_4 + xLi^+ + xe^- \rightarrow xLiFePO_4 + (1-x)\ FePO_4$ (discharge), respectively. However, the actual lithiation/delithiation kinetics between LFP and $FePO_4$ (FP) are complicated and depend strongly on the detailed reaction conditions (*e.g.* particle size and morphology, *etc.*) [116–119]. To clarify the phase transformation mechanisms, Zhu et al. reported a detailed *in situ* TEM study on lithiation of micron-sized FP crystals by using the open cell consisting of a $FePO_4$ cathode, a naturally-grown Li_2O solid electrolyte, and a Li metal anode [120]. As shown in Fig. 2f, during lithiation, a thin layer of LFP formed on the surface of FP, and a sharp step-like phase boundary (PB) developed between FP and LFP. PB was shown to be parallel to the (0 1 0) plane and moved along the [0 1 0] direction, which was also the direction of lithium ion diffusion. This might be explained by the high Li ion concentration at the right portion of the particle. Meanwhile, periodic misfit dislocations were observed on the FP side of the PB. The lattice constants of the FP and LFP phases near the PB were close to their respective stress-free values, indicating the relaxation of the elastic strain energy by the formation of misfit dislocations. These *in situ* TEM observations offer direct evidence of migration of sharp PBs in micron-sized FP/LFP systems.

Niu et al. further investigated the delithiation of the LFP nanowire electrode by using the silicon nanowire anode, and the $LiPF_6$ solid electrolyte inside the TEM [121]. Different from the sharp LFP/FP interface observed under other conditions, a disordered solid solution zone (SSZ) of Li sublattice was observed to be formed quickly on the surface of LFP, as shown in Fig. 2g. Remarkably, the nanoscale SSZ was very stable and persisted for hundreds of seconds without dislocation formation at ambient temperature, which could lead to a better cycle life of nanosized LFP in ASSLBs. Another interesting STEM study was realized by Kobayashi et al. on an oriented single crystal surface of partially chemically delithiated LFP [122]. They saw the crack formation due to changes in cell parameters. During the material relaxation, they evidenced the partial disappearance of the cracks associated to the surface deconstruction. These results further reveal the mechanisms of delithiation in LFP cathode materials.

Chalcogenic materials (sulfur/selenium/oxygen)

Sulfur is a high-potential cathode material for LIBs because of its extremely high theoretical specific capacity (1675 mA h g^{-1} based on complete conversion of S to Li_2S), moderate working potential (∼2.1 V), and remarkable energy density (2600 W h kg^{-1}), which based on the theoretical values is nearly an order of magnitude higher than that of the traditional LCO. Additionally, sulfur is one of the most abundant elements on earth, and it is nontoxic and environmentally friendly [123–126]. The challenges in Li-S batteries include dissolution of intermediate reaction products (Li_2S_x, $3 \leq x \leq 8$) into liquid electrolytes, large volume expansion (approximately 80%), and low intrinsic electronic conductivity of sulfur and Li_2S [127–129]. Thus, solid electrolytes have been used in Li-S batteries to mitigate certain inherent problems, such as the dissolution of Li_2S_x into electrolytes [130–134]. Nevertheless, the development of all solid-state Li-S batteries remains at the early stage, and systematic research on the underlying mechanisms of all solid-state Li-S batteries should be performed. Xu et al. employed various *ex situ* and *in situ* methods to study the mechanism of the Li-S redox reactions and properties of Li_2S_x and Li_2S [135]. *In situ* TEM experiments with a Li_2O serving as a solid electrolyte demonstrated that the Li diffusion into sulfur during discharge preferentially occurred at the sulfur surface and resulted in the formation of a solid Li_2S crust, which would increase cell resistance and lead to capacity degradation in Li-S batteries. In a separate report, a sulfur confined within 200 nm cylindrical inner pores of individual carbon nanotube (CNT) was used as the cathode to contact the Li metal anode with a layer of Li_2O solid electrolyte [136]. Fig. 3a shows that Li reacted with S along the axis of a CNT

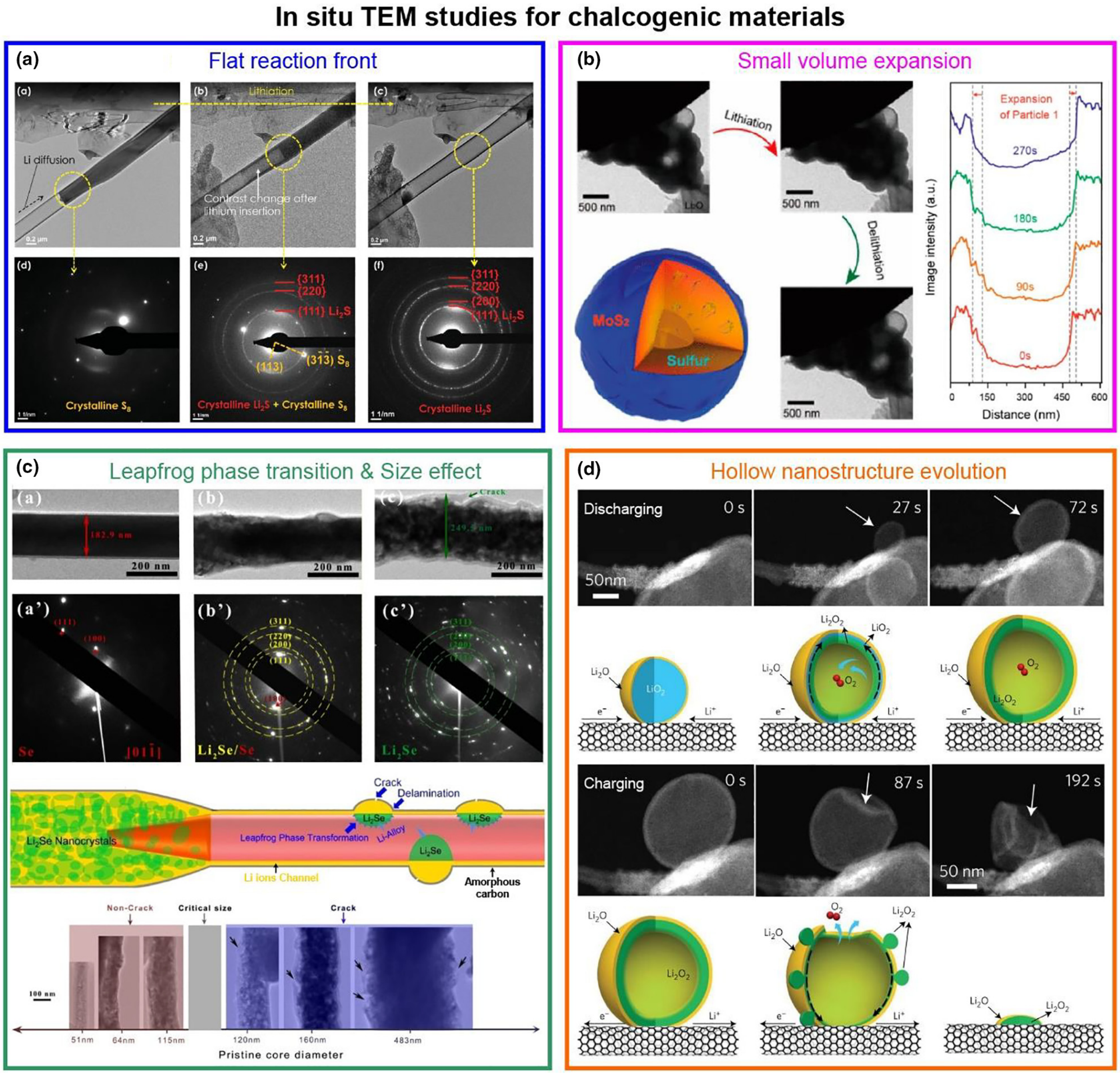

FIGURE 3

In situ TEM studies for chalcogen cathodes. (a) Flat reaction front in lithiation process of S confined within inner cylindrical pores of carbon nanotubes. Reproduced with permission [136]. (b) Small volume expansion of encapsulated S hollow nanospheres by MoS_2 flakes during lithiation. Reproduced with permission [138]. (c) Interfacial lithiation induced leapfrog phase transition and size effect in carbon coated Se cathode during lithiation. Reproduced with permission [146]. (d) Morphological evolution of the discharge–charge products for Li-O_2 nano all solid-state batteries. Reproduced with permission [46].

(*i.e.* axial lithiation) accompanied by a flat reaction front, which is different from the typical core–shell lithiation behavior of other electrode materials, on account of the formation of a conductive Li_2S/S interface. Specifically, no bulk intermediate phases (polysulfides Li_2S_n with $n = 4–8$) [137] were detected during the entire lithiation process, and the final product was only nanopolycrystalline Li_2S. This result implies that a highly undesirable polysulfide shuttle could be avoided in ASSLBs. Notably, a small volume expansion of S during lithiation was observed, which might be attributed to the relatively high mechanical strength of CNT and volatility of S under electron irradiation.

A composite structure of S cathode encapsulated by MoS_2 nanoflakes was also designed to accommodate the large volume expansion [138]. *In situ* TEM observations indicated that the sublimation of S particles could be prevented, and Li ion flowed through the Li_2O solid electrolyte layer and reacted MoS_2-encapsulated hollow S sphere leading to a 33–48% expansion of particle size which in contrast to the theoretical value of 80%, as shown in Fig. 3b. The small volume changes could be attributed to the hollow structure of S spheres that provides extra space as well as the presence of the extremely flexible MoS_2 nanoflakes. These factors can collectively facilitate the suppression of volume expansion. In addition, the lithium diffusivity in the encapsulated S was estimated to be $10^{-17}\sim10^{-16}$ m^2 s^{-1}, which matched the solid-state reaction rates in the lithiation of spatially confined sulfur in CNTs. This work strongly suggests the necessity of applying structural engineering to improve the performance of the S-based electrodes.

Selenium (Se), located in the same group as S, possesses similar chemical properties as those of S, which makes Se a promising candidate of cathode materials in ASSLBs [139–144]. The Se cathode has a lower theoretical gravimetric capacity (675 mAh g^{-1}) than S, but its volumetric capacity density (3253 mAh cm^{-3}) is comparable to that of S (3467 mAh cm^{-3}). It also has merits of greater electrical conductivity and higher output voltage. Hence, compared with Li-S batteries, Li-Se batteries could have higher energy density, improved electrochemical activity, and faster electrochemical reaction with Li. Nevertheless, similar to Li-S batteries, many challenges to Li-Se batteries need to be addressed before their practical applications, which call for fundamental research on reaction mechanisms. Using *in situ* TEM techniques, Li et al. investigated the mechanism and kinetics of lithiation reactions in the selenium nanotubes with lithium metal as the anode, and Li_2O grown on the surface of lithium metal as the solid electrolyte [145]. The nanotube was gradually expanded by approximately 88% with an H-type reaction front after the lithiation process was triggered. Meanwhile, a contrast change occurred between the reacted and unreacted areas, which was attributed to the stress/strain caused by the surface reaction, volume expansion from the reacted area, and electron beam illumination. In addition, the lithiation of Se exhibited a one-step reaction mechanism with phase transformation from single crystal Se to Li_2Se, which was similar to the lithiation of S [136].

Recently, the Li ion transport, phase transformation, and coupled chemo-mechanical effect of a uniformly carbon coated Se nanowire were studied where the solid electrolyte consisted of naturally grown Li_2O on Li metal anode [146]. Different from the H-shaped reaction front in a Se nanotube [145], a V-type reaction front was observed during lithiation of a Se@carbon nanowire, which stemmed from faster surface diffusion than bulk diffusion (radial) in Se. It was also found that Li was preferentially nucleated at certain interfacial atomic defects or weak bonds along the 1D direction before the arrival of the reaction front, suggesting a leapfrog phase transformation process of interfacial lithiation, as shown in Fig. 3c. Obviously, if the entire Se cathode was divided into numerous random sites, lithiation reaction kinetics would be accelerated through the leapfrog phase transformation. In addition, the *in situ* SAED study revealed that the Li-Se reaction product consisted of only Li_2Se without any intermediate phase, which further confirmed the findings of Li et al. [145]. Finally, they observed a threshold diameter region of Se nanowires with approximately 115–120 nm, above which the carbon coating (approximately 8.5 nm) cracked and delaminated. This study gives insights into the lithiation kinetics and size effect of the Se cathode.

Lithium-oxygen (Li-O_2) batteries that combine lightweight Li metal and abundant oxygen as active materials have received significant attention because of their high gravimetric theoretical energy densities, which can be 2–5 times larger than those of conventional LIBs [142,147–149]. Despite the advantage of Li-O_2 batteries, they suffer from many drawbacks including short cycle life, low rate capability, and poor round-trip efficiency [150,151]. The application of metal oxygen batteries is currently hampered by two major technical difficulties: One is the sluggish formation and decomposition of the metal oxides, which leads to large voltage polarization between discharge and charge, causing the low efficiency of batteries; the other is the formation of carbonates in the oxygen cathode, which electrically isolate the discharge products from the oxygen cathode and leads to battery failure. Accordingly, mechanistic insights into the Li-O_2 reaction are essential. Up to now, significant research progress has been made in understanding the reaction mechanisms of Li-O_2 batteries with liquid organic electrolytes [152–155], but limited knowledge is available on the reaction of all solid-state Li-O_2 batteries (Li-O_2 ASSLBs). Recently, the reversible reaction process of a nano Li-O_2 ASSLB was unveiled in an aberration-corrected ETEM under an oxygen environment, where the CNTs dressed with a nanosized RuO_2 catalyst were used as a cathode, Li metal as an anode and Li_2O, formed on the surface of Li metal, as a solid electrolyte [46]. As shown in Fig. 3d, in the discharge process, Li ions reacted with oxygen ($Li^+ + e^- + O_2 \rightarrow LiO_2$, $4Li^+ + 4e^- + O_2 \rightarrow 2Li_2O$) at a three-phase junction (*i.e.* contact point of CNTs, Li_2O/Li, and O_2) to generate the initial LiO_2 spheres coated with a Li_2O surface layer. Subsequently, the metastable LiO_2 immediately evolved into Li_2O_2 and O_2 through a disproportionation reaction ($2LiO_2 \rightarrow Li_2O_2 + O_2$). With consumption of LiO_2, the solid spheres gradually turned into the hollow spheres, which continued to grow because of the released O_2 gas. This condition caused the remaining shell to consist of an inner Li_2O_2 shell covered with Li_2O. In the charge process, Li_2O_2 transformed to LiO_2 by losing one Li ion and one electron ($Li_2O_2 \rightarrow LiO_2 + Li^+ + e^-$), which then released O_2 gas until complete decomposition. The hollow Li_2O_2 particles shrank and collapsed to a crumpled shell, then preferred to decompose through the formation of small Li_2O_2 particles. This hollow nanostructure evolution provides direct evidence and understanding of the reaction mechanism in Li-O_2 ASSLBs.

In addition, other *in situ* TEM observations found that the Li_2O_2 was preferentially electrochemically oxidized at the multi-walled CNT/Li_2O_2 interfaces, not at the Li_2O_2/$LiAlSiO_x$ solid electrolyte interface [156]. This condition suggests that electron transport, not Li ion transport, restricted the oxidation kinetics of Li_2O_2 at high rates or overpotentials. Thus, electron transport plays a key role in governing the rate capability of rechargeable Li-O_2 batteries. Designing electrodes to maximize the Li_2O_2/electrode interfacial area will be helpful in improving the rate capability of Li-O_2 batteries.

Metal sulfides

Transition metal sulfides have drawn great attention in the field of ASSLBs because of their higher theoretical specific capacities compared with traditional intercalation electrode materials and better electrochemical reversibility than their metal oxide counterparts [157,158]. Among those transition metal sulfides, titanium disulfide (TiS_2) pioneered by Whittingham et al. [159] is a well-known stable and high-capacity cathode material with a long cycle life [160–162]. Fu et al. combined *in situ* TEM with other methods, including DFT calculations, electrochemical tests, and synchrotron X-ray pair distribution function (PDF) analysis, to track the phase and structure evolution during the lithiation of TiS_2 [163]. In the *in situ* TEM experiments, the TiS_2 sample, Li metal, and the Li_2O formed on Li metal served as the cathode, anode and solid electrolyte, respectively. As shown in Fig. 4a, the Bragg reflections clearly exhibited a gradual negative shift from 0 s to 122 s, implying an increase of lattice parameters during Li intercalation of TiS_2. By comparing the diffraction data, the intercalation process was identified as phase transformation from TiS_2 to layered $LiTiS_2$ with no symmetry broken: the lithium ions inserted into the lattice of TiS_2 and occupied octahedral sites between Ti-S slabs, leading to the formation of covalent bonding of S-Li-S, accompanied by 0.58% and 8.5% lattice expansions of TiS_2 along *a* and *c* directions, respectively. As the Li ions were continually inserted, the conversion reaction was triggered (122 s–600 s), and it underwent the following multiple steps: $LiTiS_2 \rightarrow TiS \rightarrow Ti_2S \rightarrow Ti$. Notably, two intermediate phases were formed by the decomposition of $LiTiS_2$, as opposed to the earlier report of direct conversion reactions [164]. The corresponding structural changes were also observed at high resolution. Upon lithiation, the lattice of TiS_2 obviously expanded along the *c* direction by 12% from 0.576 nm to 0.645 nm (see HRTEM images from 0 s to 219.6 s). The different scope of observation between *in situ* SAED and *in situ* HRTEM resulted in a subtle difference in the measured lattice expansions. As a result of conversion reaction, further lithiation resulted in the generation of Ti_2S, Li_2S, and Ti phases (see HRTEM images from 238.8 s to 713.1 s), which were consistent with the analysis of *in situ* SAED. This study implies that at a very low voltage, TiS_2 can be decomposed by lithiation. This phenomenon can be prevented by increasing the low cut off voltage, though the problem of contact with Li dendrites remains.

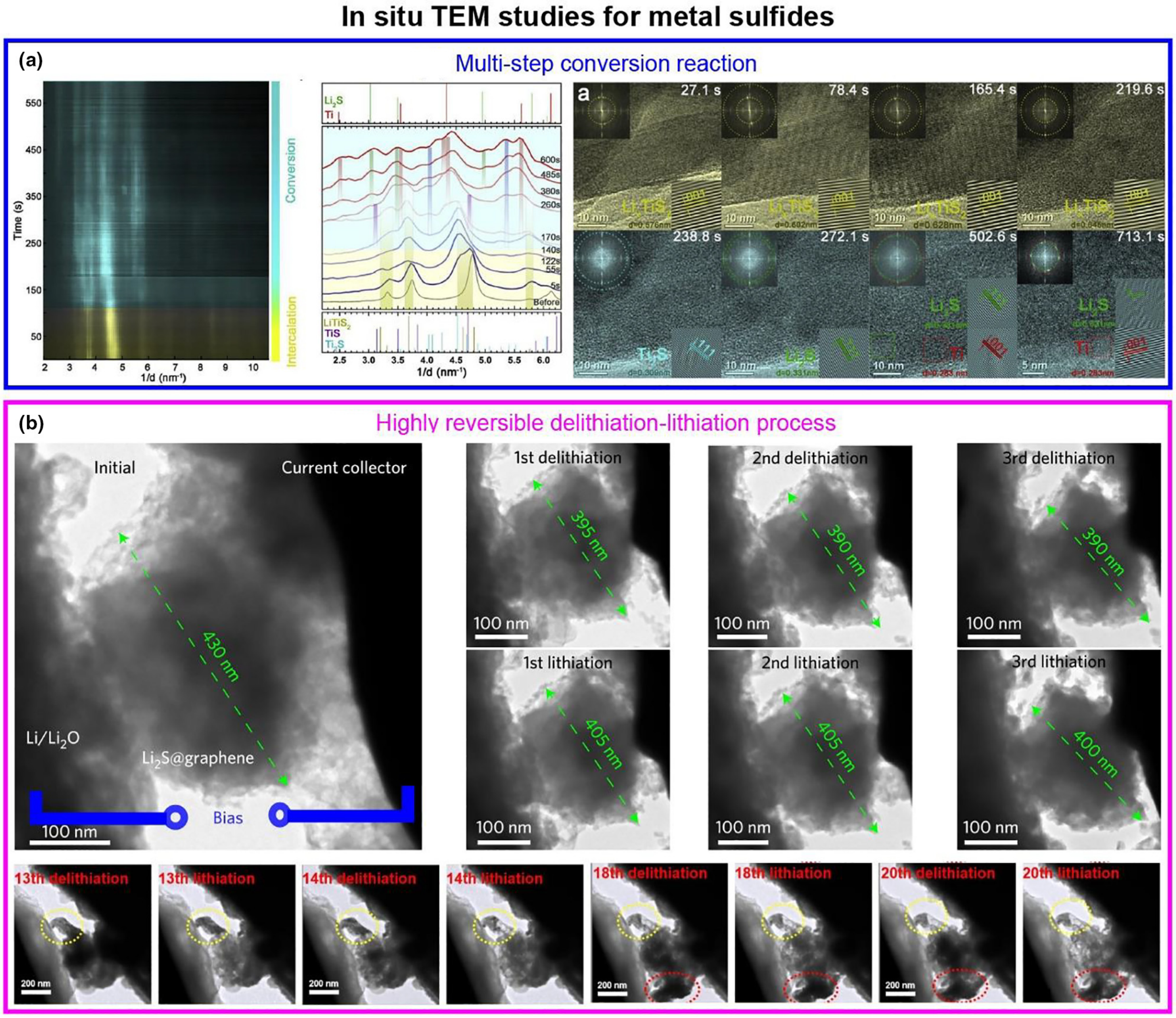

FIGURE 4

In situ TEM studies for metal sulfides. (a) Multi-step conversion reaction (as proved: $LiTiS_2 \rightarrow TiS \rightarrow Ti_2S \rightarrow Ti$) and the related reaction kinetics during expanded lithiation process in the TiS_2 at an atomic-scale. Reproduced with permission [163]. (b) TEM morphologies of Li_2S@graphene after different delithiation and lithiation cycles. The Li_2S@graphene can maintain the good structural integrity for about 20 cycles at least, showing high reversibility and structural stability. Reproduced with permission [173].

Another promising metal sulfide for ASSLBs is Li sulfide (Li_2S). It undergoes a lithiation reaction of $8Li_2S \rightarrow S_8 + 16Li$, thus delivers a high theoretical capacity of 1166 mAh g^{-1} [165–168]. In the fully lithiated phase, Li_2S is expected to have no volume expansion during cell operation, thereby ensuring the stable cycling of batteries [169,170]. More importantly, Li_2S could be paired with non-Li anodes due to the Li contained nature, such as silicon or tin-based compounds [171,172]. The main issue of Li_2S is the poor ionic and electronic conductivity and therefore the infiltration of Li_2S into conductive materials (*e.g.* carbon black or mesoporous carbon) is important. Besides the enhancement of conductivity, the effect of these conductive materials, in view of Li_2S structural stability, was also characterized by *in situ* TEM where Li_2O on the Li metal anode surface was regarded as the solid electrolyte. By studying the Li_2S/graphene nanocapsule, shown in Fig. 4b, Tan et al. observed an approximately 20% reduction compared with the initial diameter after first delithiation [173]. During following cycles, the particle showed minimal volume variation of approximately 10%, with sizes varying between 390 nm and 405 nm, which differs from the large volume expansion in sulfur cathodes. By contrast, the Li_2S without graphene coating displayed severe structural vulnerability after three cycles under the same condition. Interestingly, the Li_2S@-graphene maintained good structural integrity for approximately a dozen of cycles even at a high rate.

Metal fluorides

Because of the high theoretical energy density and working potential, transition metal fluorides were also applied as cathode materials for ASSLBs [7,174–177]. However, poor rate performance and large voltage hysteresis have plagued fluoride-based batteries. To address these problems, a better understanding of phase transformation, electron and ion transport, and reaction kinetics is urgently needed. Wang et al. studied Li transport and conversion reactions in a nano FeF_2-based ASSLB (cathode: FeF_2-C, anode: Li metal, solid electrolyte: LiN_xO_y) through a combined use of *in situ* TEM, diffraction, and spectroscopy [178]. As shown in Fig. 5a, the morphological evolution resembled a spinodal-decomposition-like process. The lithiation was initiated on the surface of the FeF_2 particles and moved rapidly across them. This process was followed by a gradual phase transformation in the bulk, leading to 1–3 nm Fe crystallites mixed with amorphous LiF. Intriguingly, the lattice parameter of the Fe particles in the near-surface region is slightly larger (by approximately 4%) than that of the particles in the central region as shown in the Fast Fourier Transform (FFT) pattern, which may result from a nano-size effect. Besides, the complete lithiation within individual FeF_2 particles was surprisingly fast (within 3–12 min), which is at variance with the conventional view that conversion electrodes show slow kinetics. These results indicate that engineering an electrode with active nanoparticles directly connected to the current collector could enable fast cycling [179], which contrasts with the traditional method of preparing heterogeneous nanocomposite electrodes that often leads to agglomerates of active materials [180–182].

Recently, Karki et al. revisited the conversion reaction mechanisms in FeF_2 during lithiation by using *in situ* TEM (LiN_xO_y served as electrolyte), and revealed a conversion-driven topotactic transformation [183]. As shown in Fig. 5b, FeF_2 particles initially exhibited the characteristic diffraction spots of single crystal. Upon lithiation, four new, broad, arc-shaped diffraction spots appeared at locations adjacent to the spots of {2 0 0} FeF_2, which represented a mosaic of tiny Fe crystallites with a fourfold symmetry (indexed to the {1 1 0} Fe family of planes). This condition indicates that the converted Fe phase was not randomly oriented as previously thought, but preferentially aligned along specific crystallographic orientations of the parent FeF_2. As the lithiation continued, Fe grains grew with the consumption of the parent FeF_2, thereby causing lattice distortion, dislocation formation, and Fe domain coarsening. As a result, the kinetics of the conversion reaction was slowed. Furthermore, an obvious shift in the peak position of the (2 0 0) FeF_2 was not observed, indicating no lattice distortion or expansion within the diffraction resolution limit.

In another work, Fan et al. built a nanobattery inside the TEM with cobalt-oxygen-doped iron fluoride nanorods ($Fe_{0.9}Co_{0.1}OF$) as the cathode, lithium metal as the anode, and Li_2O as the solid electrolyte, and discovered an intercalation-extrusion reaction in $Fe_{0.9}Co_{0.1}OF$ during lithiation [184]. As shown in Fig. 5c, a clear contrast change was observed during the Li insertion reaction, and the reaction front swept rapidly across the nanorod. Compared with the lithiation conversion reaction in the aforementioned 10–20 nm-sized FeF_2 nanoparticles, the 200 nm-sized $Fe_{0.9}Co_{0.1}OF$ displayed a much faster reaction on the surface and in the bulk (within only approximately 10 s). Meanwhile, the volume expansion in $Fe_{0.9}Co_{0.1}OF$ was smaller than that in FeF_2. After lithiation, a 1.5∼2 nm thick oxygen-rich layer was formed on the surface of the lithiated $Fe_{0.9}Co_{0.1}OF$. This surface layer was effectively stabilized by Co doping, which inhibited the reaction of electrolytes with the nascent metal nanoparticles and subsequent dissolution of transition metals into electrolytes. The combined first-principles calculations and experimental characterizations further revealed that anion and cation co-substitutions could reduce the conversion reaction potential and shift the reaction from a less reversible intercalation-conversion reaction in iron fluoride to a more reversible intercalation-extrusion reaction with fast reaction rate and small volume expansion, thereby significantly improving the battery performance. This co-substitution strategy offers a new way to address similar reversibility problems encountered by other conversion reaction materials in ASSLBs.

In this section, we have summarized the representative *in situ* TEM studies on cathode materials of ASSLBs including Li transition metal oxides and polyanionic compounds, chalcogenic materials, and metal sulfide/fluoride. Generally, there are three reaction mechanisms dominating Li ion storage in these cathodes, *i.e.* intercalation, alloying, and conversion. (i) Li transition metal oxides and polyanionic compounds are the typical intercalation cathodes, and it is highly desired that they work without obvious structural degradation during ion insertion/extraction. However, many kinds of defects have been reported in these cathodes during electrochemical cycle by *in situ* TEM, such as coherent twin boundaries and antiphase domain boundaries (LCO, LNMO), dislocations (LFP, Li_2MnO_3), and stacking faults (Li_2MnO_3). These localized structural changes during Li ion insertion/extraction will lead to the structural degradation of

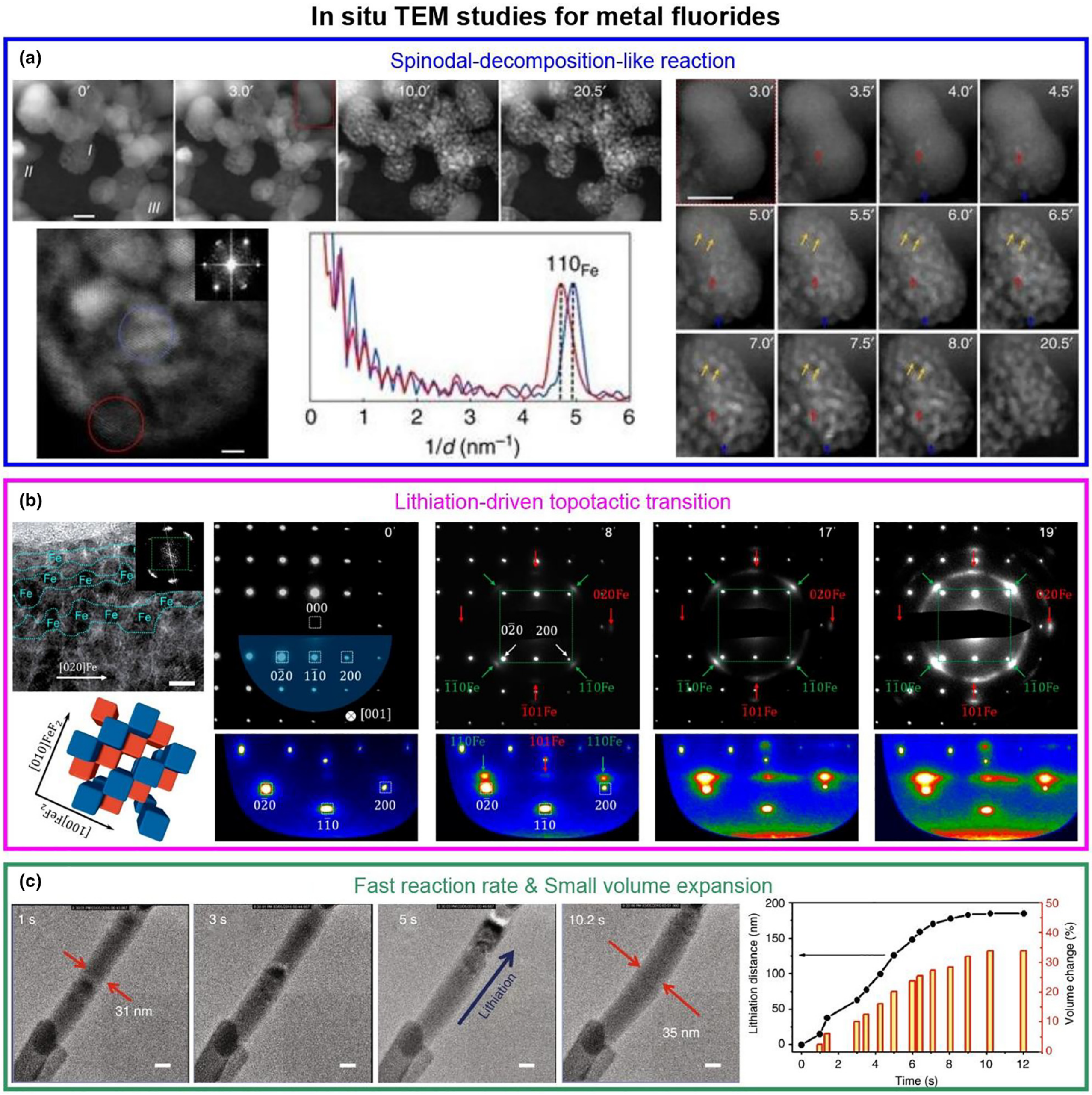

FIGURE 5

In situ TEM studies for metal fluorides. (a) Spinodal-decomposition-like reaction in lithiation process of FeF_2. The lithium conversion was initiated at the surface, sweeping rapidly across the FeF_2 particles, followed by a gradual phase transformation in the bulk, resulting in 1–3 nm iron crystallites mixed with amorphous LiF. Reproduced with permission [178]. (b) Lithiation-driven topotactic transition in FeF_2, creating a checkerboard-like structure, within which the volume change is largely compensated. Reproduced with permission [183]. (c) Fast reaction rate (within ~10 s) and small volume expansion (~35% with a little bend) of a 200 nm $Fe_{0.9}Co_{0.1}F$ nanorod in lithiation process. Reproduced with permission [184].

cathodes or lager lithium transfer resistance, and thus cause the fast-capacity decay upon cycling and poor rate performance. Inspired by such discoveries, structural and compositional modification (particle size reduction, optimization of the interfacial nanocrystal orientation, and atomic scale elemental doping or substitution, *etc.*) could be the promising strategies to improve the ASSLB performance of these cathodes. (ii) In contrast to intercalation cathodes, the chalcogenic materials possess more high theoretical specific capacity based on the complete alloying reaction of M to Li_2M (M = S, Se, O_2). The poor kinetics, large volume expansion and shuttle effect are the common problems during electrochemical cycle in chalcogenic cathodes. Notably, *in situ* TEM results demonstrate that no intermediate phases are formed during the lithiation process of S and Se, which means the shuttle effect could be well suppressed within all solid-state Li-S/Se batteries. Meanwhile, *in situ* TEM results also prove that the hollow electrode designs can effectively control the volume expansion, and carbon-coating can facilitate the kinetics and restrain the volume expansion. (iii) For metal sulfides, *in situ* TEM studies show that their reaction mechanisms involve both intercalation and conversion processes, which depends on the discharge voltage. At a low voltage, the conversion reaction will be triggered, thus leading to the decomposition of electrodes, which could be prevented by increasing the low cut off voltage. (iv) Similar to metal sulfides, the intercalation-conversion mechanisms have been identified in metal fluorides by *in situ* TEM, where the conversion reaction plays the dominant role during electrochemical cycle. *In situ* TEM studies further reveal that the intercalation-conversion mechanism can be shifted into an intercalation-extrusion via anion-cation cosubstitution strategy, which could enhance the reversibility and cyclability of metal fluoride cathodes.

In situ TEM studies of Li metal anodes

As Li metal has the highest theoretical capacity (3860 mAh g^{-1} or 2061 mAh cm^{-3}) and lowest electrochemical potential (−3.04 V versus that of the standard hydrogen electrode) of all possible candidates, it is regarded as the "holy grail" of anodes for ASSLBs [12,185,186]. Unfortunately, safety concerns caused by dendrite growth and low Coulombic efficiency during charge/discharge cycles seriously limit the practical use of Li metal anodes [187–189]. Therefore, profound understandings of interfacial chemistries, Li deposition behavior, and the correlations between them are needed to address these issues.

Li metal deposition mediated by Au seeds

Rational design of Li hosts is a promising approach to accommodate the large volume changes of Li metal during cycling. Metal nanoparticles (such as Au, Ag, and Mg) with zero overpotential of Li nucleation have been proven to be effective in regulating Li deposition in carbonaceous host materials. Cui's group reported a nanocapsule structure composed of hollow carbon nanospheres (HCNSs) inside Au nanoparticle seeds for spatial control of Li metal deposition [190]. *In situ* TEM observations were performed in a solid cell arrangement with nanocapsule as the cathode, Li metal as the anode and a native layer of Li_2O as the solid electrolyte. The results showed that Li can fill HCNSs under the assistance of Au nanoparticles without depositing outside the carbon shell (Fig. 6a). It was also shown that, the Li filling process was reversible; the Au nanoparticles precipitated again onto the inner wall of carbon spheres in a different shape when Li was stripped out of the nanocapsules. By contrast, Li dendrites grew outside the carbon shell of HCNSs without Au nanoparticles. As graphene exhibits higher mechanical stability, improved Li ion conductivity, and much stable solid electrolyte interphase (SEI) than that of amorphous carbon spheres, Cui's group further proposed the wrinkled graphene cages (WGC) with Au seeds composite structures as the Li host [191]. *In situ* TEM observations demonstrated a similar Li deposition behavior to that of HCNSs with Au seeds, where Li_2O served as the solid electrolyte (Fig. 6b). These substrate-dependent Li metal nucleation phenomena provide direct evidence that Li metal can be encapsulated in the enclosed space with the aid of heterogeneous seeds. Thus, Li metal plating/striping was isolated from the electrolyte to reduce the chemical side reactions and improve the electrochemical cycling stability of the Li metal anode. These studies provide a simple and feasible strategy for fabrication of Li metal anodes with high stability.

In situ TEM was also employed to study the detailed mechanism of Li metal nucleation and growth as well as its interaction with heterogeneous seeds during cycling. For example, Wang's group investigated the plating/stripping of Li metal within a confined amorphous carbon nanotube embedded with gold NPs (Au@*a*-CNT) inside the TEM using L_2O as the solid electrolyte [192]. They proposed a front-growth mechanism to explain the spatially confined Li growth and stripping. As shown in Fig. 6c, an Au nanoparticle (labeled as Au-1) inside an *a*-CNT first reacted with Li to form the Li-Au alloy upon lithiation, accompanied by pronounced volume expansion. Then, the Li metal nucleated on the Li-Au alloy surface and rapidly plated upward and downward along the axial direction of this *a*-CNT. Finally, the hollow interior of the nanotube was filled by Li metal grown from Au seeds. It was also observed that a different Au nanoparticle (labeled as Au-2) did not alloy with Li, which can be explained by the sufficiently large confinement from the *a*-CNT. In the stripping process, the Li metal was gradually stripped out of the nanotube interior under a reverse bias, accompanied by simultaneous shrinking of the Li-Au alloy. With the extraction of Li, Au atoms precipitated from the Li-Au alloy to form a cluster, giving a clear contrast change. The dissolved Au atoms precipitated as separate clusters elsewhere apart from the original particle. Thus, different from the first Li deposition, Li metal can nucleate and grow upward from the bottom of the tube with the aid of the precipitated Au clusters due to short ion diffusion distances. The *in situ* SAED showed that Au reacts with Li to form an intermediate phase of $LiAu_3$ during the early stage of lithiation due to insufficient Li supply, and further lithiation leads to the transition from $LiAu_3$ to a fully lithiated phase of Li_3Au. During stripping of Li metal, Li_3Au was reversibly converted to $LiAu_3$ and further dealloyed, to become an Au cluster, which is consistent with observation of the contracted particle with a reduced size and darker contrast. This reversible two-step alloying reaction is different from a previous report on the reaction product of Li_3Au only. Furthermore, by comparing three different Li deposition processes with Au nanoparticles inside and outside an *a*-CNT and without Au nanoparticles, it was found that the nanotubes without gold seeds inside exhibited uncontrolled dendrite-like Li growth outside the carbon shell. Thus, the Au nanoparticles inside the nanotube hollow interior play an important role in aiding Li growth. In addition to the Li metal, the Au-seed-aided growth may be applied to encapsulate the sodium metal in the future. These results provide mechanistic insights into heterogeneous-seeds-aided Li nucleation and space-confined Li deposition for the design of high-performance Li metal anodes.

Li metal deposition without seeds

The development of Li hosts without nanoseeds has also drawn much attention, since the use of noble metal is accompanied with high cost and complex preparation procedures. Cui's group reported layered reduced graphene oxide (rGO) as a stable host for Li metal anodes [193]. The *in situ* TEM observations indicated that the Li metal uniformly deposited between rGO layers via the L_2O solid electrolyte (Fig. 7a), which was attributed to increased nucleation sites and nearly full interfacial protection by rGO lay-

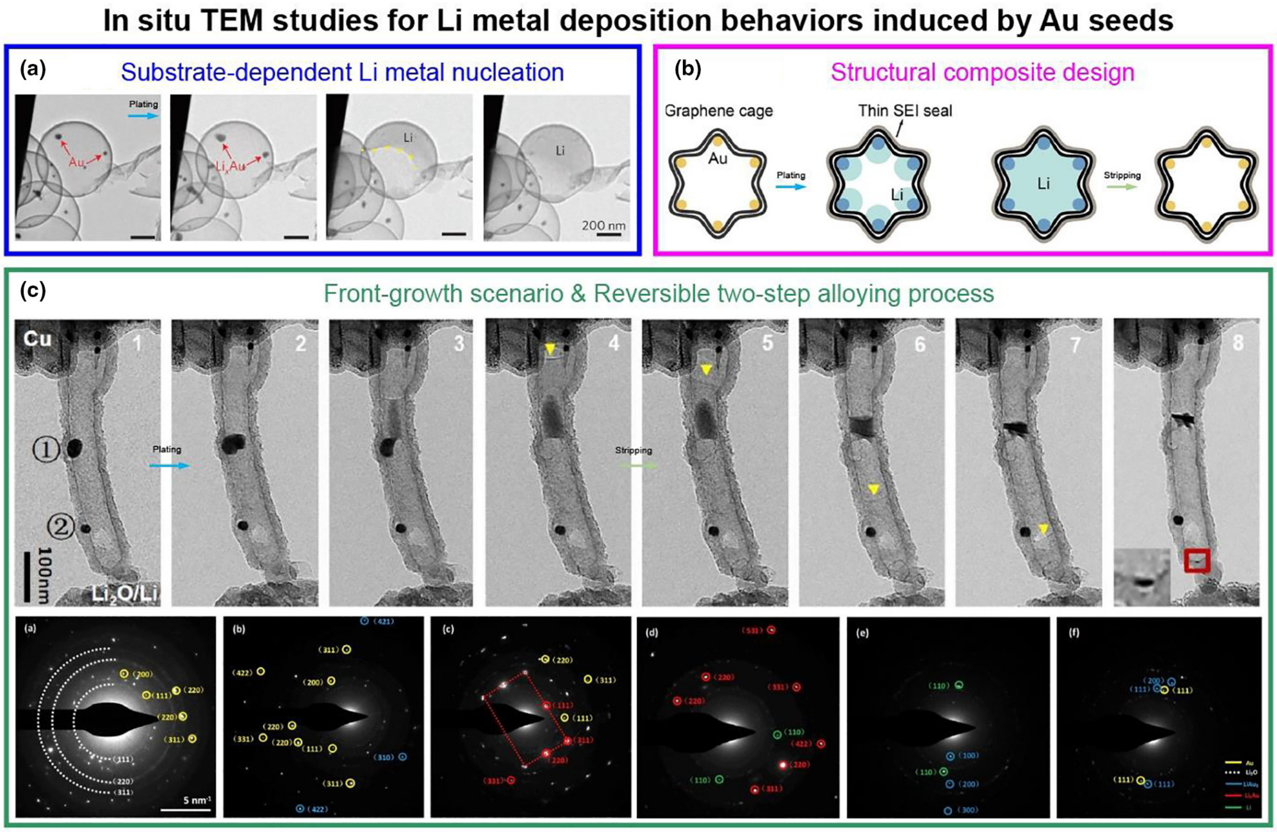

FIGURE 6

In situ TEM studies of Li metal deposition induced by Au seeds. (a) Selective deposition of Li metal in Au@HCNSs. No Li deposition was observed outside the carbon shell until all the connected nanocapsules were fully filled under the induction of Au seeds, and the Li deposition process was reversible. Reproduced with permission [190]. (b) Schematic of Li metal deposition in Au@WGC. Li deposition took place inside the hollow space of WGC. Reproduced with permission [191]. (c) Front-growth mechanism and reversible two-step alloying process (plating: Au → $LiAu_3$ → Li_3Au, stripping: Li_3Au → $LiAu_3$ → Au) during Li metal deposition of Au@*a*-CNT. Reproduced with permission [192].

ers. After Li deposition, rGO had minimal thickness changes, suggesting excellent dimensional stabilization of layered rGO hosts.

Liu et al. also reported a novel crumpled graphene ball (CGBs) as Li host without nanoseeds [194]. Fig. 7b shows the *in situ* Li deposition in CGBs using L_2O as the solid electrolyte. Dendritic growth was not observed during Li plating, demonstrating that as long as appropriate nucleation sites are provided, Li metal can also be deposited in some carbon-based hosts without Au seeds, thereby giving stable dendrite-free Li metal anodes. Matthias et al. designed a solid polymer electrolyte open cell (see Fig. 1) and conducted the *in situ* monitoring of the reversible intercalation of lithium into bilayer graphenes (BG) [51]. From the time series of TEM images in Fig. 7c, a clear reaction front was observed inside the BG, and grains were discerned by different colors. The Fourier-filtered TEM images offered a direct view of the encapsulated crystal, where different contrasts indicated different thicknesses within a single grain. The EELS analysis further indicated that the crystalline phase formed during lithiation likely consisted of pure Li, which agrees with the results from the Fourier transform of TEM. Furthermore, the Li crystal can be extracted from BG during delithiation, showing good reversibility. First principles calculations also suggested that the formation of a multilayer close-packed Li phase between graphene sheets was feasible. Evidently, the Li storage capacity in the close-packed Li phase intercalated between graphene sheets can lead to a structure with Li content greatly in excess of LiC_6. These *in situ* TEM results not only demonstrate direct visualization of the intercalation behavior of Li in BG, but also point out the possible existence of distinct storage arrangements of Li ions in 2D layered materials compared with their bulk counterparts.

Recently, Wang's group designed a nitrogen-doped hollow porous carbon sphere (N-HPCS) and used it as the host for protection of lithium metal anodes [195]. *In situ* TEM experiments (Li_2O served as the solid electrolyte) demonstrated that these N-HPCS enabled the Li metal to be encapsulated in a highly reversible and repeatable manner. As shown in Fig. 7d, the pristine N-HPCS was first fully lithiated during plating as evidenced by its volume expansion and shell thickening. Thereafter, the Li metal started to nucleate inside the nanosphere, and then filled in the hollow space of N-HPCS through two possible pathways (1 and 2 in a_2) with a clear boundary. The SAED patterns and dark-field (DF) image further confirmed that a single-crystal Li particle occupies almost the entire hollow space of the sphere. When a reverse bias was applied, the deposited Li was gradually stripped out of the cavity, which caused the shrinkage of N-HPCS to its original size. The subsequent SAED pattern revealed that the Li-containing species can be completely extracted without

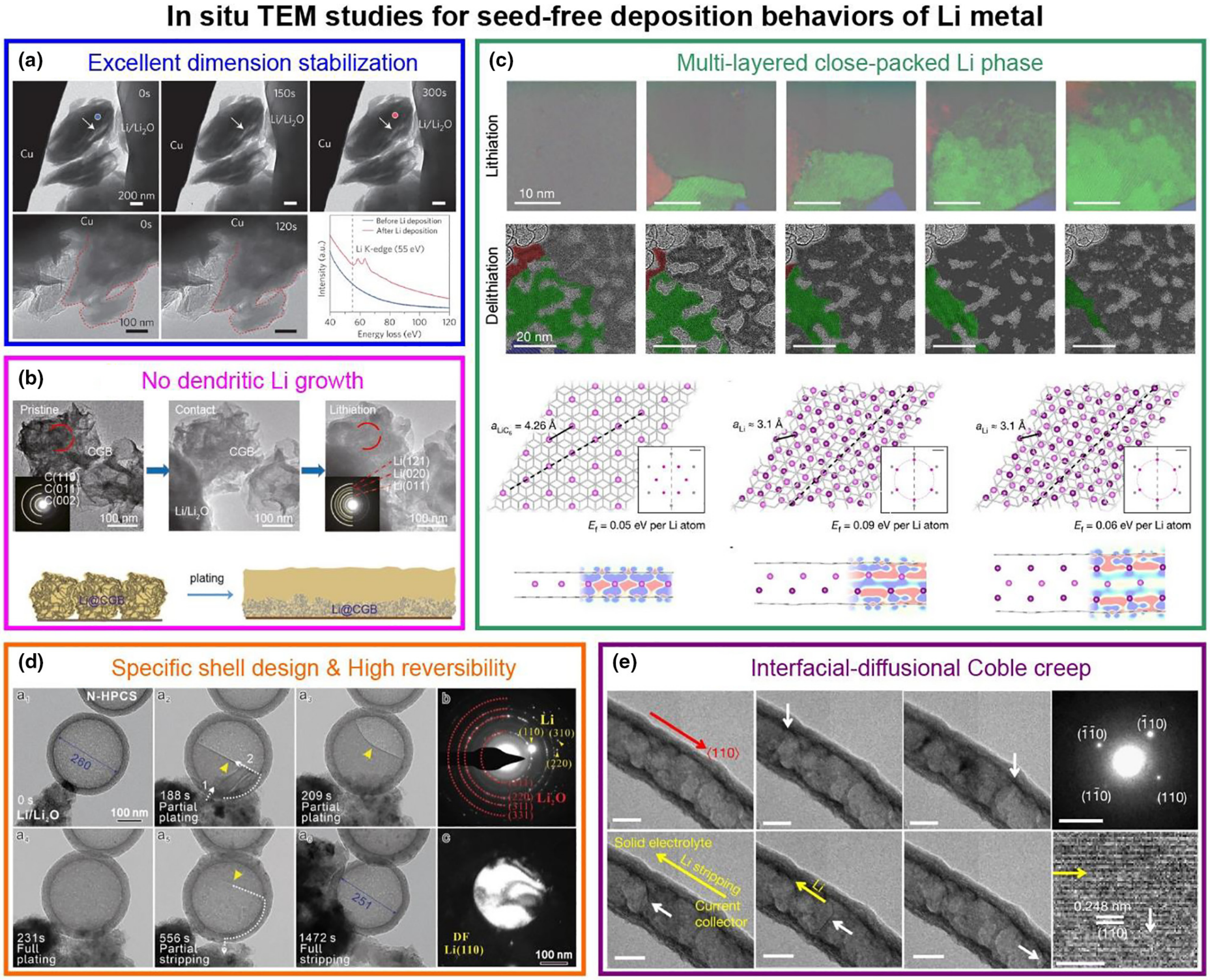

FIGURE 7

In situ TEM studies for seed-free deposition behaviors of Li metal. (a) Excellent dimension stabilization during Li metal deposition in rGO. The highly increased nucleation sites and the nearly full interfacial protection by the rGO layers leaded to the uniform Li deposition. Reproduced with permission [193]. (b) No dendritic Li growth during Li metal deposition in CGB. Reproduced with permission [194]. (c) Multi-layered close packed Li phase deposition in BG. Reproduced with permission [51]. (d) Specific shell (N-HPCS) design for Li deposition hosts with high reversibility. The thin N-rich denser layer on the inner surface of shell induced preferential nucleation of Li inside the hollow sphere. Reproduced with permission [195]. (e) Interfacial-diffusional Coble creep during Li metal deposition in MIEC. The Li plating/stripping was highly reversible. Reproduced with permission [196].

residue after stripping. The plating/stripping of Li metal can be repeated inside the N-HPCSs, and a long Li plating/stripping cycle (up to 50 cycles) was achieved, showing an excellent cycling stability of N-HPCSs. Besides, they also compared the Li deposition behavior of other types of carbon spheres with modified shell structures, including HPCSs (less N) and N-HCSs (less pores), and found that both carbon spheres failed to encapsulate Li and eliminate the dendrite. Therefore, high-level N doping and rich nanopores are essential for building a lithiophilic carbon shell favorable for Li ion penetration.

In another work, Li's group proposed a 3D carbonaceous solid host structure that consisted of mixed ionic-electronic conductor (MIEC) tubules, which are electron-conductive, Li-conductive, and lithiophilic [196]. They demonstrated plating/stripping of Li or Na inside individual carbon tubules by using *in situ* TEM, where a ~ 50 μm thick polyethylene oxide (PEO)-based polymer was used as the solid electrolyte. As shown in Fig. 7e, a distinct MIEC/metal phase boundary was formed in tubules during the Li deposition process, and the SAED pattern revealed strong diffraction spots of Li metal, indicating its single crystal structure feature. Li can also be stripped along the tubules, showing an excellent cycling stability of MIEC. They proposed three possible paths for Li diffusion: MIEC wall, interface between an MIEC wall and Li_{bcc}, and bulk Li_{bcc}. Theoretical calculations showed that the dominant mechanism of Li deposition and stripping was the interfacial diffusional Coble creep instead of bulk diffusional Nabarro-Herring creep. Remarkably, through interfacial diffusional Coble creep, the stress could be effectively relieved, the electronic and ionic contacts could be maintained, and the solid-electrolyte interphase debris could also be eliminated, thereby achieving the reversible deposition/stripping of Li over many cycles. These findings shed light on the harnessing the complex diffusion process for Li metal deposition/stripping.

Growth mechanism and mechanical stress of Li metal

In addition to the design of conductive, lightweight and lithiophilic hosts to mitigate Li decomposition during cycling and inhibit dendrite growth, extensive efforts have been devoted to stabilize Li electrodes by controlling the geometry or surface of Li metal anodes using various additives (*e.g.* CO_2, HF, iodide, benzene, organic compounds, or wax) or by mechanical modification and design [197–199]. Recently, Huang's group reported the preparation of air stable Li spheres (ASLSs) by electrochemical plating under a CO_2 atmosphere inside an ETEM [200]. As shown in Fig. 8a, the Li sphere nucleated at the CNT (cathode), Li_2O (solid electrolyte), and CO_2 triple point and continuously grew with time, forming a core–shell structure with a Li core and a Li_2O/Li_2CO_3 shell. Notably, the morphology of the Li sphere remained after exposure to ambient air for 30 min, and the SAED patterns from the sphere before and after air exposure were similar, *i.e.* both only contained the diffraction rings of Li_2CO_3, Li_2O, and sharp diffraction spots of Li. This phenomenon demonstrates that the Li sphere with a surface layer of Li_2CO_3 is stable in air, which can be rationalized by the protection of Li_2CO_3 due to the insolubility of Li_2CO_3 in water and inertness with oxygen and nitrogen at room temperature. Furthermore, they also constructed a nanobattery consisting of an air-exposed ASLS anode, a Li_2CO_3/Li_2O solid electrolyte, and an Au-coated CuO nanowire cathode inside an ETEM to test whether the air-exposed ASLSs can be used as an anode for Li based batteries. Reaction front and volume expansion can be observed in time-resolved TEM images, and SAED patterns confirmed the formation of Li_2O, Cu, and LiAu, which is highly similar to the electrochemical behavior of the CuO nanowire observed using fresh metallic Li as the anode [201], indicating the feasibility of ASLS anode and demonstrating that the surface Li_2CO_3 layer is a good Li ion conductor. In particular, compared with Li foil, ASLS has a higher surface area and is more stable in air. Thus, ASLS can efficiently reduce the true current density during charge/discharge to avoid dendrite growth, improving the safety and efficiency of Li batteries. This study provides a new strategy for the preparation of air-stable Li metal anodes.

The key to the practical application of the Li metal anode is to suppress Li dendrite formation. Tremendous efforts have been devoted to suppress Li dendrite growth and prime examples include building an artificial SEI, use of solid electrolytes and modifying electrolyte systems. Clearly, without an in-depth understanding of the fundamental sciences for the Li dendrite formation and interaction with the separator, safe operation of Li metal batteries remains elusive. Very recently, He et al. directly captured the nucleation and growth behavior of Li dendrites under elastic constraint by coupling an atomic force microscopy (AFM) cantilever into a solid open-cell set-up at a controlled gas environment (approximately 10^{-2} mbar CO_2) inside the ETEM [48]. Fig. 8b shows a typical process of Li dendrite formation from the onset of Li deposition (nucleation) to dendrite growth and final failure associated with increased compressive forces due to dendrite elongation. As indicated in the figure, Li deposition started with the formation of a faceted Li particle at the interface between the Li_2O solid electrolyte and working electrode with no preferential growth directions. A dendrite then sprouted out of the interface between the Li_2O solid electrolyte and Li particle and grew at a considerable rate (up to approximately 256 nm s^{-1}). Interestingly, as soon as the dendrite sprouted out, the growing dendrite pushed the particle upward, suggesting that the deposition of Li happened locally at the Li whisker/solid electrolyte interface, which indicated a tip-growth model. Overall, the real-time observation of transition from uniform particle growth to dendrite growth demonstrated in this work has implications for potentially controlling the deposition of Li metal by tailoring the initial SEI chemistry and pressure within the cell.

Similarly, Huang's group also directly captured the nucleation and growth of Li dendrite with simultaneous stress–strain measurement by using the ETEM-AFM platform [47]. They were able to control the *in situ* growth of Li dendrites with diameter of a few hundred nanometers and simultaneously measure the elastic–plastic properties of individual Li dendrites with and without electrochemical driving forces, as shown in Fig. 8c. One breakthrough from this work is the novel use of ETEM that overcomes a long-standing challenge to measure the basic electro-chemo-mechanical properties of extremely reactive materials such as Li. Novel electro-chemo-mechanical coupling phenomena have been revealed in this work. It can be understood that the Li dendrite problem in ASSLBs is neither pure mechanical nor pure electrochemical, which is governed by the coupling of mechanics and electrochemistry. For example, the yield stress of bulk lithium is less than 1 MPa, however, the mechanical stress generated by Li deposition in solid state electrolyte can reach GPa level [47,196]. That is to say, electrochemical overpotential driven Li deposition can generate much greater stress than the yield stress of lithium. As such, when studying Li mechanics in ASSLBs, it needs to be investigated in the context of the electrochemical environment. Inside the gas environment of ETEM, a nanometer-thick Li_2CO_3 forms on the surface of *in situ* grown Li dendrites. Such an ultra-thin Li_2CO_3 layer remarkably stabilizes the reactive Li metal and prevents electron-beam damage, thereby enabling *in situ* imaging and mechanical testing. Owing to the protection of surface Li_2CO_3, they obtained the first experimental results on the mechanical properties of Li dendrites, and the results are unprecedented and unexpected. The ETEM-AFM platform is innovative because the AFM tip plays a three-fold role: (a) serving as a cathode; (b) axial confinement to generate growth stress; and (c) real-time measurement of growth stress. This platform can be extended to study dendrites in sodium, potassium, magnesium, and calcium battery systems, and offer the information of the stress-mediated growth of reactive materials at the nanoscale. The results on the elastic–plastic properties of Li dendrites are extremely important because they represent the first set of robust experimental data on the previously unknown mechanical behavior of the Li dendrites. This findings provide baseline data for verification and validation to a vast amount of theoretical models on the mechanical behavior of Li dendrites with and without electrochemical driving forces.

In this section, we have summarized the representative *in situ* TEM studies on plating/stripping of Li metal, the growth and associated electro-chemo-mechanical behavior of Li metal

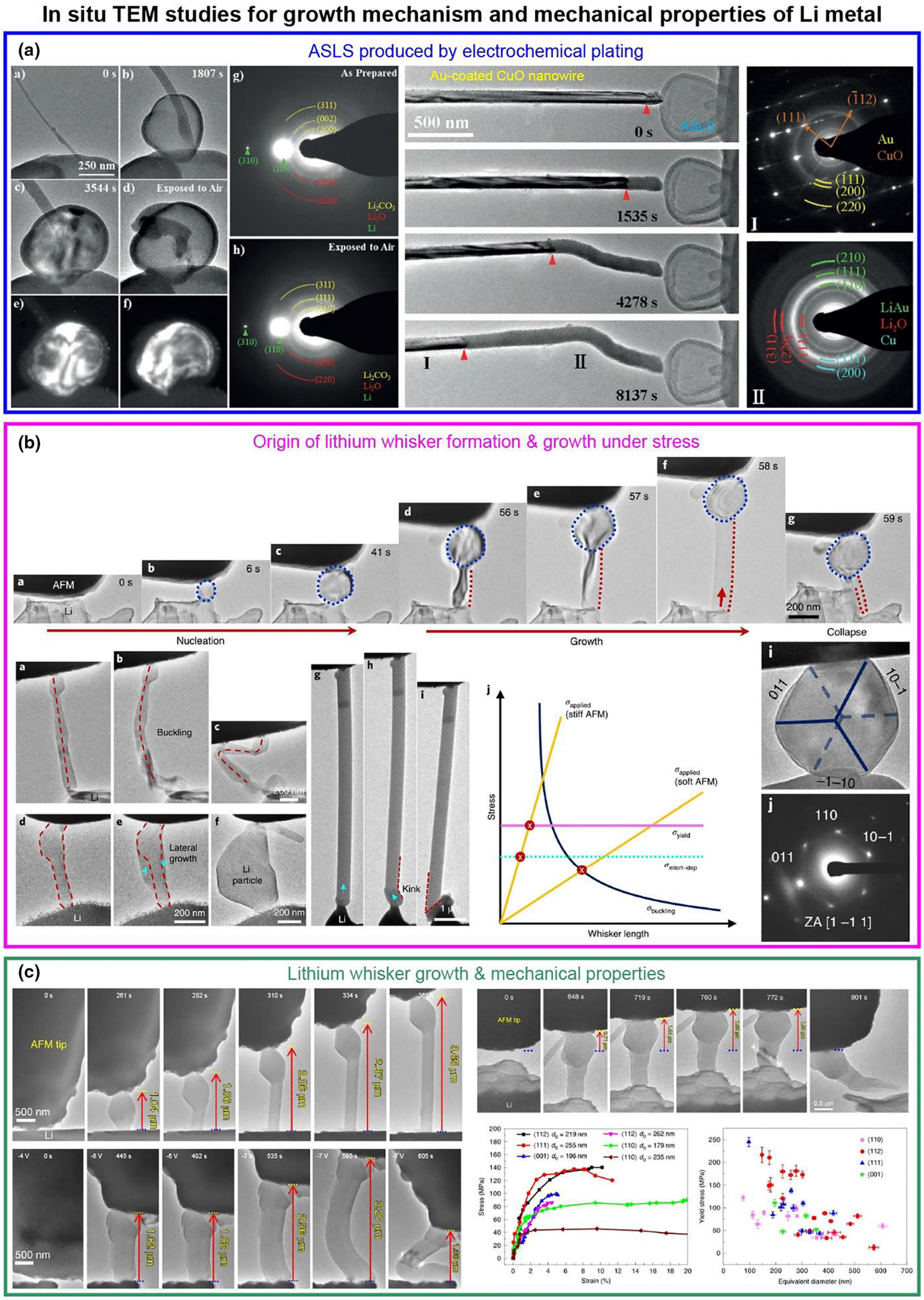

FIGURE 8

In situ TEM studies for growth mechanism and mechanical stress of Li metal. (a) ASLS produced by electrochemical plating. The ASLS is stable upon air exposure for 30 min, and can be used as anodes for Li-ion batteries, which confirmed by the lithiation of CuO nanowire inside the TEM. Reproduced with permission [200]. (b) Origin of lithium dendrite formation and growth under stress. A single crystalline Li particle with no preferential growth directions was firstly deposited, then a Li whisker sprouted out at the contact point, and pushed the particle upward. Reproduced with permission [48]. (c) Li dendrite growth and mechanical stress. The growth stress could reach up to 130 MPa, and the measured yield strength of Li whiskers under pure mechanical loading reaches as high as 244 MPa. Reproduced with permission [47].

anodes. (i) The safety issue caused by the fatal Li dendrite formation seriously impedes the application of Li metal anodes. Therefore, how to reduce local current density, uniformize Li ion flux and regulate the Li plating/stripping behaviors is of great importance for preventing dendrite growth. *In situ* TEM studies demonstrate that Li metal can be uniformly nucleated through the guide of lithiophilic nanoseeds (*e.g.* Au nanocrystals). It is also worth noting that Li dendrites can be suppressed by rational morphology design of Li hosts, even without nanoseeds. Additionally, the diffusional Coble creep has been identified in a solid-state battery during Li plating/stripping by *in situ* TEM. (ii) In a broad class of ASSLBs, one approach to suppress Li dendrite growth has been the use of mechanically stiff solid electrolytes. However, Li dendrites still grow through them. Therefore, it is necessary to understand the growth mechanism and mechanical stress of Li dendrite. *In situ* TEM studies show that the morphology of Li metal can be well controlled under CO_2 atmosphere to form lithium spheres and Li whiskers. The lithium spheres can be used as stable anodes in air, due to the protection of ionic conductive Li_2CO_3 layer. Remarkably, the elastic–plastic properties of individual Li whiskers are tested by the AFM tip, which provide quantitative benchmarks for the design of Li dendrite growth suppression strategies in ASSLBs.

In situ TEM studies of electrode/solid electrolyte interfaces

Solid electrolyte is a core component of ASSLB and thus critically controls the performance of ASSLB, including energy density, power density, cycle stability, safety, temperature-dependent performance, and service life [14,15,202]. During the past several decades, great progress has been achieved in the development and optimization of solid electrolytes [203–205], and the ionic conductivity of certain solid electrolytes (*e.g.* $Li_{10}GeP_2S_{12}$ and Li_2S-P_2S_5) is comparable to or higher than that of liquid organic electrolytes. However, ASSLBs have not reached the desired power densities comparable to liquid electrolyte-based batteries [133]. This is in part due to high interfacial resistances between electrodes and solid electrolytes, which hinders the transport of Li ions and limits the power densities of ASSLBs [21,206]. To address this problem, extensive effort has been devoted to reduce the interfacial resistances including contact resistance and nanoionic resistance in recent years [207–210]. However, the mechanism underlying the high Li ion transfer impedance remains unclear. To improve the performance of ASSLBs, it is crucial to develop fundamental understandings of the interfacial processes during charge/discharge.

Cathode/electrolyte interfaces

$Li_{1+x+y}Al_yTi_{2-y}Si_xP_{3-x}O_{12}$ (LATSPO) is a promising solid electrolyte, which is not only chemically stable but also exhibits the ionic conductivity over 10^{-4} S cm^{-1} at room temperature [211]. By using *in situ* TEM, Yamamoto et al. directly observed the change of electric potential near the LCO cathode- LATSPO solid electrolyte interface during charge/discharge cycling (a gold film was acted as the anode) [212]. Electron holography (Fig. 9a) shows that the potential in LCO has a relatively linear slope, with a steep drop at the interface, while a gradual slope was observed in the LATSPO near the interface. By contrast, the potential in the electrolyte far from the interface did not change at all, regardless of the voltage, indicating that the resistance mainly arises from regions near the interface. This 2D potential distribution was attributed to the movement of Li ion near the interface, which was confirmed by EELS results: Co^{3+} oxidized to Co^{4+} by Li extraction from LCO during charging.

By applying the operando STEM-EELS mapping with the hyperspectral image analyses of the non-negative matrix factorization (NMF) and SA/SB method, Nomura et al. dynamically and quantitatively observed the interfacial phenomena between the LCO cathode and $Li_{1+x+y}Al_x(Ti, Ge)_{2-x}Si_yP_{3-y}O_{12}$ (LASGTP) electrolyte during charge and discharge reactions inside the TEM [213]. As shown in Fig. 9b, the nano ASSLB was composed of a LCO cathode/a LASGTP solid electrolyte/an Au anode. A non-uniform Li ion distribution was found in the charge/discharge process, indicating the non-uniform extraction/insertion of Li ion. This phenomenon could be attributed to the activity of the electrochemical reaction that depended on the pristine-state Li ion concentration. In addition, an electrochemically inactive region (10–20 nm thick) was formed between the LCO and LASGTP interface, which was identified as the mixture of LCO and Co_3O_4 by the STEM-EELS, SAED, and Raman spectroscopy. The spinel Co_3O_4 has a low ion conductivity, thus resulting the high interfacial resistance of Li ion transfer. In a very recent work, Nomura et al. further investigated the Li distribution in the interface between the LCO cathode and LASGTP electrolyte by using sparse coding (SC) method, and demonstrated that the SC reconstruction could significantly improve the temporal resolution with a sufficient signal-to-noise ratio (SNR), even for the low-SNR Li maps recorded at a higher scanning speed [214]. Fig. 9c shows the nanometer-scale spatial variation of the Li concentrations in the LCO cathode at different stages during charge and discharge reactions, where the Li ions can move along both the parallel and vertical directions to the LCO/LASGTP interface. Interestingly, Li ions also can diffuse inside LCO film even under the open-circuit condition. These results not only provide an in-depth understanding of the LCO/LASGTP interface in the charge and discharge processes, but also demonstrate the feasibility of using this new method for elucidating the phenomena of solid-state electrochemistry in non-equilibrium states.

Li-phosphorus oxynitride (LiPON) is one of the successful examples of ceramic electrolytes, which possesses a moderate mechanical strength but low ionic conductivity ranging from 10^{-8} to 10^{-6} S cm^{-1} [215]. Santhanagopalan et al. fabricated a nanoscale ASSLB consisting of LCO cathode, Si anode, and LiPON electrolyte inside the TEM and investigated the interfacial chemical changes in charged and overcharged batteries [216]. They found that LCO showed high Li accumulation in a pristine sample, and increased Li accumulation at the LCO/LiPON interface for the charged and overcharged samples. Interestingly, the Li accumulation at Si/LiPON and Si/Cu interfaces were also evident in the overcharged sample, and attributed to the phosphorus-silicon interdiffusion and possible Li plating. These findings highlight the importance of interfacial engineering in ASSLBs to improve the reversibility of Li insertion, thereby giving good cycling and high rate performance.

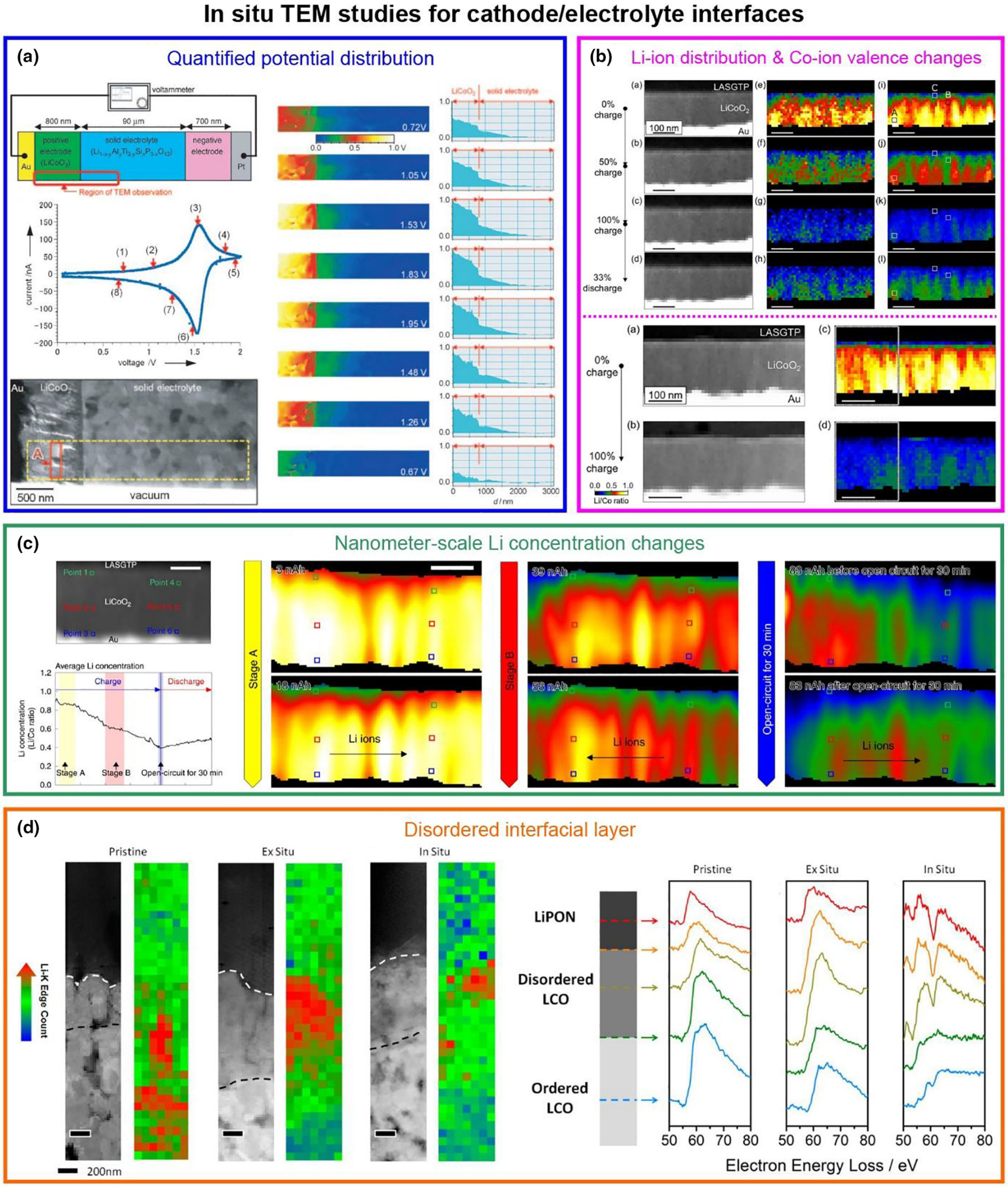

FIGURE 9

In situ TEM studies for cathode/electrolyte interfaces. (a) Quantified potential distribution between LCO and LATSPO. The potential has a steep drop at the interface, indicating the a high interfacial contact resistance. Reproduced with permission [212]. (b) Li ion distribution and Co-ion valence changes in LCO/LATSPO interface. The Li ion distribution was non-uniform in the charge/discharge process, and Co_3O_4 was formed near the interface. Reproduced with permission [213]. (c) Nanometer-scale Li concentration changes in LCO cathode at different stages during charge/discharge reactions. The Li ions can diffuse along the parallel and vertical directions to the interface. The diffusion of Li ions inside LCO was also found under the open-circuit condition. Reproduced with permission [214]. (d) Disordered interfacial layer between LCO/LiPON under pristine, *ex situ* and *in situ* conditions. Reproduced with permission [50].

Wang et al. further investigated the nanoscale interfacial phenomena in LCO/LiPON/Si ASSLB using *in situ* STEM/EELS [50]. They found that an unexpected interfacial layer was formed between LCO/LiPON after cycling in both *ex situ* and *in situ* samples. The integrated radial intensity of SAED pattern demonstrated that this interfacial layer was composed of a highly disordered solid-solution of Li_2O and CoO with the rock-salt structure, suggesting that the LCO near LiPON is chemically unstable and decomposes to form an ionically resistive layer during charging. Fig. 9d shows the STEM image and EELS characterization for the pristine, *ex situ*, and *in situ* samples. Compared with the pristine sample, the *ex situ* sample had a significant integrated intensity in the disordered LCO layer, which is consistent with the previous report where *ex situ* Li accumulation was observed at the LCO/LiPON interface. Integrated intensity mapping of the *in situ* sample also exhibited increased counts in the disordered layer indicating that Li accumulation occurred during charging. Additionally, they discovered that the increase in thickness of the disordered interfacial layer rendered more electrochemically inactive cathodes, thereby resulting in rapid capacity decay. These results provide direct evidence that the mechanism of interfacial impedance at the LCO/LiPON interface is due to chemical changes rather than space charge effects.

Anode/solid electrolyte interfaces

Na super ionic conductor (NASICON)-type solid electrolytes are another promising class of materials with relatively high ionic conductivity (approximately 10^{-4}–10^{-3} S cm^{-1}) [203,217]. Among them, $Li_{1+x}Al_xGe_{2-x}(PO_4)_3$ (LAGP) has been widely investigated because of its relatively wide electrochemical window [218,219]. A recent study reported that LAGP readily reacted with Li at room temperature, thereby leading to fracture of LAGP [220]. However, the underlying mechanisms for the interphase formation and degradation have not been identified, which is important in stabilizing the Li/LAGP interface. To address this issue, Lewis et al. investigated the (electro) chemical reaction mechanism between Li and LAGP through *in situ* TEM and *ex situ* techniques [221]. As shown in Fig. 10a, once the LAGP contacted with Li, LAGP underwent approximately 38% volume expansion due to intercalation of Li, and the crystalline LAGP turned into an amorphous interphase. Obviously, the volume expansion caused the evolution of mechanical stress within bulk LAGP pellets and eventually induced fracture. These findings not only reveal the key degradation and failure mechanisms in LAGP, but also provide in-depth understanding of the solid electrolytes that form non-passivating interphases in contact with Li. This is the main problem of most solid electrolytes, which are thermodynamically unstable against Li metal.

$Li_{1.3}Al_{0.3}Ti_{1.7}(PO_4)_3$ (LATP) is another NASICON-type solid electrolyte, which is also easily reduced by Li metal [222]. To enhance the stability of these kinds of solid electrolytes, developing an interface with good chemical and mechanical stability, which possesses high electronic insulation and ionic conductivity, has been demonstrated to be a feasible strategy to effectively alleviate the degradation of solid electrolytes [223,224]. For example, Cheng et al. successfully fabricated LATP pellets coated a thin boron nitride (BN) layer (~5–10 nm) by chemical vapor deposition [225]. To study the protective effect of nanoscale BN coating, they observed the reaction between LATP (LATP/BN) and Li metal in real-time by *in situ* TEM. The results show that the LATP firstly underwent an intercalation reaction to form the $Li_3Al_{0.3}Ti_{1.7}(PO_4)_3$ during lithiation. As insertion of Li ions went on, the $Li_3Al_{0.3}Ti_{1.7}(PO_4)_3$ was gradually reduced to form an amorphous phase. The drastic volume changes eventually cause the cracking of LATP particle, which was similar to the lithiation in LAGP [221]. In sharp contrast, the LATP/BN particle did not occur distinct structural change when reacting with Li for 1 h, except the slight change in diffraction pattern, as shown in Fig. 10b, which demonstrate that the reduction of LATP by Li can be prevented by the nanoscale BN coating. This work exhibits the extraordinary protective effect of nanoscale boron-nitride coating for LATP, and offers a good choice to stabilize other solid electrolytes against Li.

Very recently, Zhu et al. further studied the chemo-mechanical failure mechanism on the LATP based ASSLBs by using X-ray diffraction, solid-state nuclear magnetic resonance (NMR), and *in situ* TEM [226]. As shown in Fig. 10c, up on delithiation, spherical-like lithium clusters deposited slowly at the contact interface at first. Soon after, many lithium clusters began to come out directly from LATP, and grew along the surface of LATP nanorod over time. This phenomenon can be associated with the formation of the interphase with high electronic conductivity. The high electronic conductivity leads to some local sites with lower critical potential that are beneficial to lithium deposition [223], which then caused the chemical degeneration of LATP. As for lithiation process, the SAED patterns in Fig. 10c demonstrated that the pristine well-crystallized LATP quickly transformed into amorphous phase upon Li ions insertion, consistent with Cheng's work [225]. In addition, an obvious bending deformation occurred in the LATP nanorod during lithiation, which was attributed to the anisotropic volume expansion. This phenomenon indicates that large stress has generated inside the LATP nanorod. Once the accumulated stress exceeds the yield limit of the LATP, the LATP eventually occurs fracture, leading to a high resistance. These findings shed light on the chem-omechanical degradation mechanism of the Li/LATP interface, which could facilitate the understanding of interfacial problems for other solid electrolytes.

Among the numerous high-performance solid electrolytes, the garnet-structured cubic $Li_{7-3x}Al_xLa_3Zr_2O_{12}$ (*c*-LLZO) has attracted great attention due to the coexistence of excellent stability against Li metal and a relatively high ionic conductivity (approximately 10^{-4} S cm^{-1}) [227]. Many theoretical calculations and *ex situ* experiments of Li/*c*-LLZO interfacial stability and conduction have been reported but remain controversial. Direct experimental observation of the Li/*c*-LLZO interfaces is the key to solving the puzzle. Recently, Ma et al. *in situ* constructed the Li/*c*-LLZO interfaces inside an aberration-corrected STEM and revealed the chemical and structural progression [228]. Notably, in contrast to conventional methods used for interface studies, they proposed a new *in situ* formation strategy of interface that the electron beam was used to sculpt Li to exclude the influence of possible lithium oxides before the *in situ* STEM observation. As shown in Fig. 10d, c-LLZO underwent a localized phase transition rather than decomposition reaction when in contact with Li metal, thereby forming an approximately 6 nm interfacial layer, which had been overlooked in prior cyclic voltammetry or X-ray diffraction experiments. The imaging and spectroscopy results showed that this interfacial layer consisted of a single phase instead of the multiple phases proposed by recent theoretical calculations, and tetragonal *c*-LLZO (*t*-LLZO) would be the most likely candidate for the interfacial layer at Li/LLZO, which contains the same elements as in *c*-LLZO except for a slightly increased Li concentra-

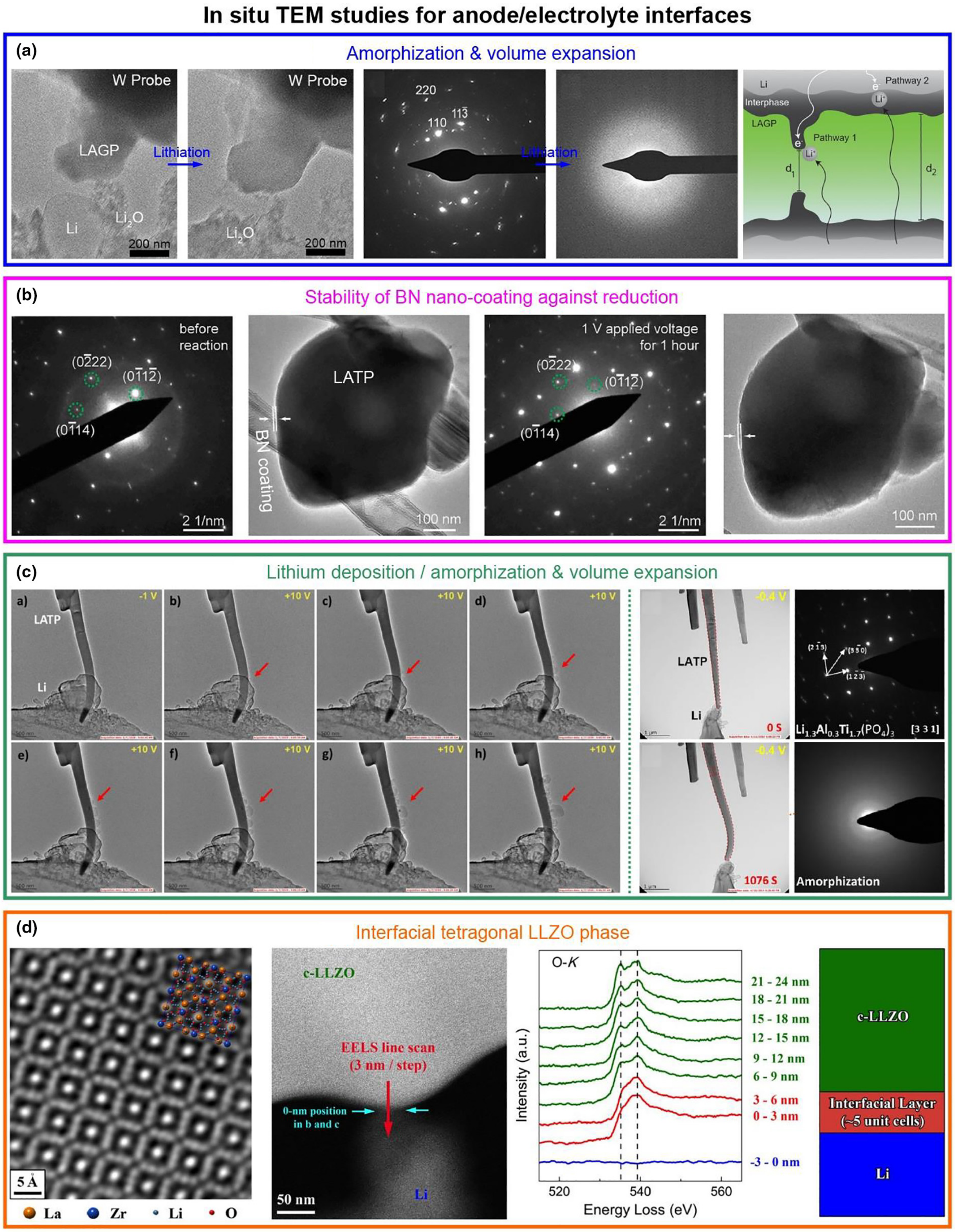

FIGURE 10

In situ TEM studies for anode/electrolyte interfaces. (a) Amorphization and volume expansion in reaction of Li and LAGP. Reproduced with permission [221]. (b) Protective effect of nanoscale BN coating for LATP. The particle and the BN coating were intact after a 1 h reaction and the diffraction pattern still matched with LATP. Reproduced with permission [225]. (c) Lithiation-delithiation process of LATP and reaction between Li metal and LATP. Lithium deposition initially occurred at the contact interface, and then lithium clusters soon began to come out directly from LATP over time. Amorphization and volume expansion were occurred during reaction. Reproduced with permission [226]. (d) Formation of interfacial tetragonal LLZO phase between Li and cubic LLZO. Reproduced with permission [228].

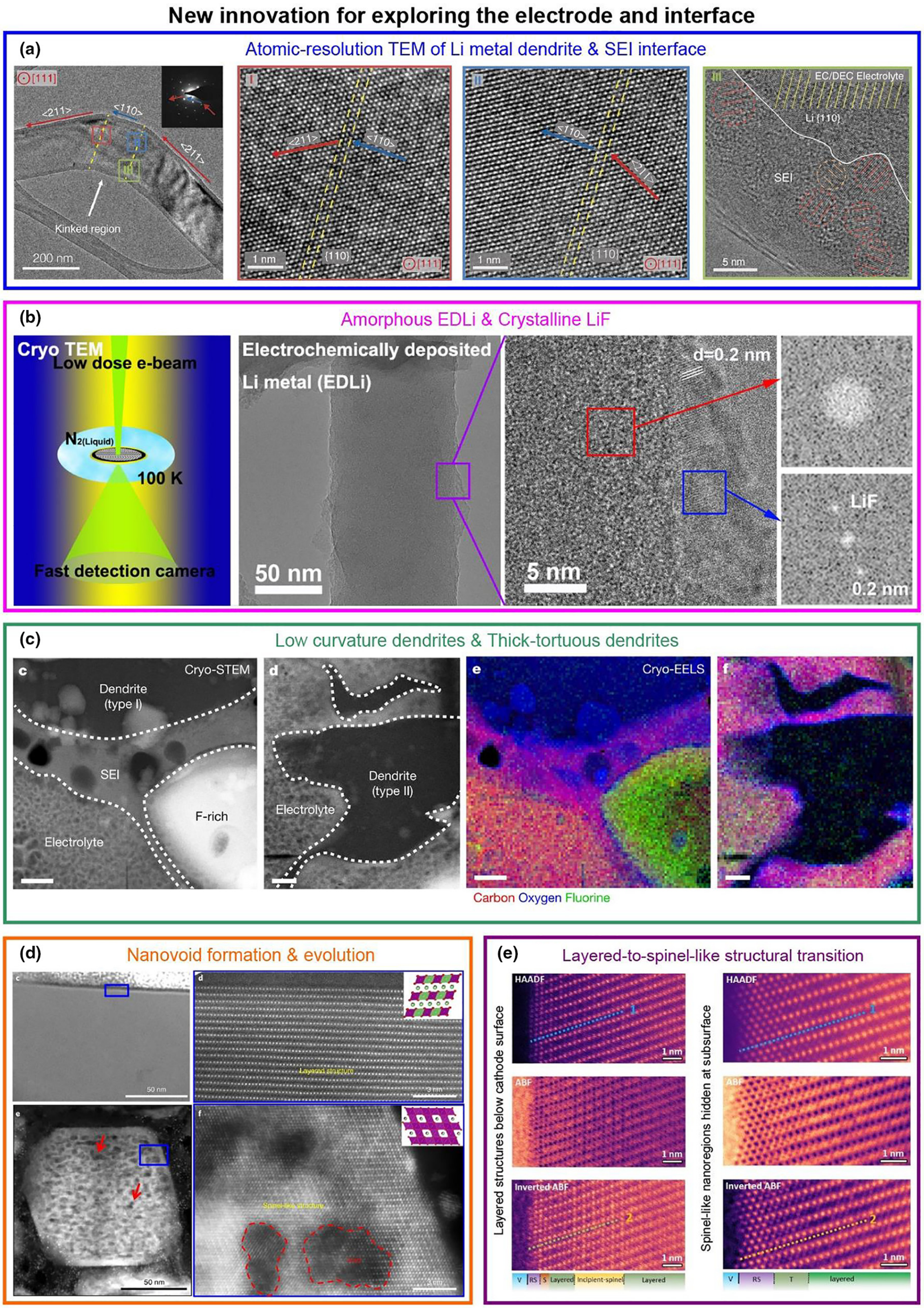

FIGURE 11

Emerging TEM techniques for characterization of battery materials and interfaces. (a) Atomic-resolution TEM images of Li metal and SEI interface. Reproduced with permission [229]. (b) Structure of EDLi and its SEI. Reproduced with permission [230]. (c) Structure and elemental composition of dendrites and their interphase layers. Reproduced with permission [231]. (d) Structural degradation of $Li_{1.2}Ni_{0.2}Mn_{0.6}O_2$ cathode. Reproduced with permission [232]. (e) Layered-to-spinel-like structural transformation in layered oxide cathode. Reproduced with permission [233].

tion. Interestingly, this *t*-LLZO-like interphase stopped growing almost immediately after its formation and became stable at a thickness below five garnet unit cells. This passivation prevented *c*-LLZO from being completely reduced by Li while maintaining facile Li ion transport, thereby explaining the good compatibility of *c*-LLZO with Li metal. These findings not only provide more in-depth information about Li/*c*-LLZO interfaces but also open a new window for designing Li-solid electrolyte interfaces that can enable the use of Li metal anodes in ASSLBs.

In this section, we have summarized the representative *in situ* TEM studies on cathode/electrolyte and anode/electrolyte interfaces. (i) For cathode/electrolyte interfaces, the electrode/electrolyte interfacial resistance has been considered a major limiting factor for improving ASSLBs performance. *In situ* TEM demonstrate that the origin of high interfacial impedance is mainly due to the decomposition of cathode materials to form an ionically resistive layer, such as the Co_3O_4 near LCO/LATSPO interface, CoO near LCO/LiPON interface. (ii) For Li metal anode/electrolyte interfaces, the decomposition reactions between Li metal and solid electrolyte is the main cause of poor performance of ASSLBs. *In situ* TEM studies elucidate the degradation and failure mechanisms in Li/LAGP and Li/LATP interfaces. Additionally, *in situ* TEM in Li/LLZO interface also demonstrate that passivation tetragonal-like LLZO layer can effectively prevent the c-LLZO from being completely reduced, without significantly weakening the ionic conductivity. These studies indicate that designing a structurally similar, stable and ionically conductive polymorph on solid electrolyte surface could be served as a promising strategy for high-performance ASSLBs.

Emerging TEM techniques for characterization of battery materials and interfaces

The traditional *in situ* TEM technologies can be effectively used to characterize the microscopic processes of most battery materials. However, characterizing the electron beam sensitive materials such as metallic Li, Na, or S-based electrolytes is extremely difficult. For example, it is difficult to obtain the atomic-scale images of Li dendrites using conventional TEM, since the morphology and structure of Li dendrites can be severely damaged under a normal TEM electron beam dose for a short period. Hence, developing novel TEM techniques to study materials with high sensitivity to electron irradiation is urgently needed. Inspired by the preparation of biological samples for cryogenic TEM (cryo-TEM), Cui's group deposited Li metal dendrites on a TEM copper grid by a conventional electrochemical method, and then cleaned off the surface liquid electrolyte, and quickly placed them in liquid nitrogen [229]. With this procedure, they were able to obtain the *post mortem* atomically-resolved images of Li metal and its interface with SEI (Fig. 11a). The Li metal dendrites characterized in this manner could be kept stable for over 10 minutes under a low dose of electron irradiation.

Similarly, as shown in Fig. 11b, Meng et al. developed a novel cryo-TEM method to probe the nanostructure and chemical composition of electrochemically deposited Li metal [230]. They found that the short plating time (5 min at 0.5 mA cm^{-2}) of Li metal in the conventional liquid electrolyte (1 M $LiPF_6$ in EC/EMC) resulted in an amorphous phase of electrochemically deposited Li (EDLi) with an uneven SEI distribution on its surface, and the crystalline LiF was present in the SEI. Interestingly, the surface property of EDLi was closely related to the additives in electrolytes, leading to the generation of various SEIs and Coulombic efficiencies during electrochemical cycling.

Kourkoutis et al. further conducted the structural and chemical mapping of solid–liquid interfaces in Li metal batteries by adapting the cryo-TEM technique [231]. They identified two dendrite types coexisting on the Li anode by freezing the liquid electrolyte to maintain the original characteristics of the solid–liquid interface of the electrode, as shown in Fig. 11c. One type of Li dendrite is approximately 5 μm in diameter, which has a small curvature and has an expanded solid electrolyte interface membrane. Another type of Li dendrite is approximately several hundred nanometers, which is curved and does not have an expanded solid electrolyte interface film. However, a Li hydroxide layer existed outside with a thickness of approximately 20 nm, disproportionately contributing to the loss of battery capacity.

Clearly, the above studies demonstrated that cryo-TEM opened new opportunities of tackling critical problems in batteries such as SEIs and Li dendrites. In addition to cryo-TEM, high-resolution STEM-HAADF imaging has also been used to reveal the battery failure mechanism in recent years. Yan et al. showed that the defects generated at the particle surface are continuously pumped into the bulk lattice for layered Li transition metal oxides (L*TMO*) by obtaining a series of atomic-resolution STEM-HAADF images [232]. They found that during the operation of a rechargeable battery, oxygen vacancies produced on the surfaces of Li-rich layered cathode particles migrate toward the interior lattice (Fig. 11d). The STEM-HAADF observation offers a unique opportunity to understand the bulk lattice degradation of L*TMO* cathodes.

Using atomic-level STEM-HAADF imaging, Li et al. reported an incipient state for layered-to-spinel-like structural transformation in the L*TMO* [233]. Surprisingly, this transformation was initiated from the subsurface layer rather than the free surface or inner edge of the surface rock salt structures, as shown in Fig. 11e. The EELS analysis further revealed that the origin of the structural transformation could be attributed to a non-uniform composition distribution at the nanoscale subsurface region. These results shed light on the hidden subsurface reconstruction and its atomic origin in LTMO cathodes.

Recently, some new TEM techniques are emerging and evolving rapidly, including integrated differential phase-contrast (iDPC), geometric phase analysis (GPA), four-dimensional (4D) STEM and etc. The iDPC function of the STEM-HAADF obtains the HADDF and ABF images simultaneously, enabling the atomic scale precision in identifying the atom positions of heavy and light elements in one image [234]. In addition, GPA was also widely employed to obtain the dislocation strain fields from the experimental as well as the simulated micrographs [235]. Moreover, 4D STEM has been applied to study the strain mapping of the electrodes [236,237]. In the near future, these new techniques will play essential roles for the studies of ASSLBs.

Finally, we note that the above new electron microscopy technologies have been mainly used for investigation of the operation and failure mechanisms of electrode materials in liquid electrolytes. In the future, a synergistic integration of these advanced *in situ* electron microscopy with new nanodevices is critical for enabling the development of innovative ASSLB platforms for the fundamental study of coupled electro-chemical-mechanical phenomena and underlying mechanisms in ASSLBs.

Conclusions and outlook

To summarize, we provided a comprehensive review of recent *in situ* TEM studies of electrodes, solid electrolytes, solid electrolyte/electrode interfaces and their interphases in ASSLBs, by covering their chemical and structural evolution, phase transformation, size effect, reaction kinetics and dynamic interfacial behavior. A fundamental understanding was provided for the mechanisms of electrochemical reaction, degradation and failure in ASSLBs during electrochemical cycling. Next we identified pressing research needs for further studies and innovation of ASSLBs via *in situ* TEM.

(1) Most current *in situ* TEM setups of nanoscale battery cells use Li_2O as a solid electrolyte, which differs from the practical solid electrolytes in macroscopic ASSLBs. Hence, the phenomena and mechanisms revealed by *in situ* TEM results may not directly reflect those in macroscopic cells. In the future, it is necessary to improve the design of *in situ* TEM setups that combine commonly-used electrodes and solid electrolytes in macroscopic ASSLBs.

(2) Almost all *in situ* TEM setups of nanoscale battery cells can only be tested for a few charge/discharge cycles and thus cannot reveal the evolution and degradation of materials and interfaces over long term cycling. To address this issue, new *in situ* TEM techniques, in conjunction with accelerated tests, should be developed to enable the real-time studies over long cycles.

(3) *In situ* TEM tests of electrochemical reactions are usually conducted under applied potentials. However, the actual overpotentials driving electrochemical reactions depend sensitively on the contact conditions between the electrode materials and electrolytes. Hence, it is difficult to quantitatively determine the overpotential and its relationship with measured reaction kinetics during *in situ* TEM experiments. To circumvent this problem, *in situ* cells with a three-electrode configuration is important to be developed to enable the quantitative measurement of nanoscale electrochemistry.

(4) A (damaging) influence of electron beam on electrochemical reactions is inevitable during *in situ* TEM experiments. This may cause artifacts in the observed phenomena and mechanisms in ASSLBs. Hence, there is a need to design a proper reaction environment that not only allows the transmission of electron beam but also closely represent the real battery working condition, given the limited space in the TEM chamber.

(5) For the solid/solid interfaces in ASSLBs, the formation of space-charge layers at heterogeneous interfaces is believed to play an important role in achieving the high performance of ASSLBs. However, the understanding of space-charge layers is limited due to the lack of experimental techniques that can be used to directly characterize their dynamic formation and evolution. Advanced 4D-STEM with *in situ* biasing could be adapted to conduct the dynamic measurement and analysis of spatiotemporal evolution of interfacial charge densities under cycling conditions.

(6) The evolution of SEI and CEI layers during electrochemical cycling is known to be a key factor that controls the electrochemical performance of conventional LIBs. However, little is known for SEI layers in ASSLBs. Currently, it is imperative to develop a nanoscale battery platform suitable for the *in situ* TEM characterization of formation, growth and properties of SEIs and CEIs between solid electrodes and electrolytes during electrochemical cycling.

(7) Although *in situ* TEM provides atomic scale structural and compositional information regarding the electrochemical reaction mechanisms of ASSLBs, most current *in situ* TEM experiments were conducted under a voltage control mode, and current control or galvanic charge/discharge mode is not attainable due to the extremely small current associated with a single nanowire or nanoparticle electrode. Furthermore, the critical electrochemical properties measurements are missing in the current *in situ* TEM experiments. As such, concurrent measurement of structural evolution with electrochemical properties of ASSLBS by *in situ* TEM is one of the grand challenge that we are facing in the evolving field.

(8) Lastly, given the aforementioned limitations of *in situ* TEM studies for ASSLBs, it remains a great challenge to simultaneously characterize all the spatiotemporal evolution of solid electrodes, solid electrolytes and their interfaces and interphases in terms of variations of composition, structure, transport and mechanical properties during electrochemical cycling. Multimodal approaches combining *in situ* techniques like TEM, Neutron scattering, X-ray diffraction, Raman, *etc.* in conjunction with computational modeling, can be applied to obtain a more complete and in-depth understanding of the material and interface problems in ASSLBs.

The above topics are a few among a vast list of potentially intriguing directions for future research. Given the rapid development of TEM technologies, *in situ* TEM studies will continue to advance our fundamental understanding of material and interface problems in ASSLBs in the coming decade. Mechanistic insights and new design guidance developed will enable the optimization and innovation in the ASSLBs field toward making next-generation high-performance rechargeable batteries.

Declaration of Competing Interest

The authors declare that they have no known competing financial interests or personal relationships that could have appeared to influence the work reported in this paper.

Acknowledgments

This work is supported by the National Natural Science Foundation of China (Grants No. 52072323, 21703185, 51872098, 61471307, 51772262, 21406191, 21935009, 51401239, 52022088, 51971245 and 11575154), the National Key Research and Development Program of China (Nos. 2018YFB0905400, 2018YFB0104300 and 2017YFB0702001), the Leading Project Foundation of Science Department of Fujian Province (Grants No. 2018H0034), Hebei One-Hundred Talent Program (Grant No. 4570028), and the High-Level Talents Research Program of the Yanshan University (Grant 005000202) and the "Double-First Class" Foundation of Materials and Intelligent Manufacturing Discipline of Xiamen University. Prof. M. Winter and Prof. J. Li acknowledge German Research Foundation (DFG, project Li 2916/2-1) for the funding support. Funding support from Beijing Natural Science Foundation of China-Haidian Special Project (L182065), Beijing Natural Science Foundation of China (2202046) and Hebei Natural Science Foundation (B2020203037) is also greatly acknowledged.

References

[1] S. Chu et al., Nat. Mater. 16 (2016) 16–22.
[2] M. Winter et al., Chem. Rev. 118 (2018) 11433–11456.
[3] B. Dunn et al., Science 334 (2011) 928–935.
[4] D. Larcher, J.M. Tarascon, Nat. Chem. 7 (2015) 19–29.
[5] C.P. Grey, J.M. Tarascon, Nat. Mater. 16 (2016) 45–56.
[6] C. Liu et al., Mater. Today 19 (2016) 109–123.
[7] F. Wu, G. Yushin, Energy Environ. Sci. 10 (2017) 435–459.
[8] R. Schmuch et al., Nat. Energy 3 (2018) 267–278.
[9] J.B. Goodenough, Y. Kim, Chem. Mater. 22 (2010) 587–603.
[10] N.S. Choi et al., Angew. Chem. Int. Ed. 51 (2012) 9994–10024.
[11] H. Kim et al., Chem. Soc. Rev. 42 (2013) 9011–9034.
[12] D. Lin et al., Nat. Nanotech. 12 (2017) 194–206.
[13] J. Betz et al., Adv. Energy Mater. 9 (2018) 1803170.
[14] A. Manthiram et al., Nat. Rev. Mater. 2 (2017) 16103.
[15] C.W. Sun et al., Nano Energy 33 (2017) 363–386.
[16] P.G. Bruce et al., Nat. Mater. 11 (2011) 19–29.
[17] R. Chen et al., Chem. Rev. 120 (2020) 6820–6877.
[18] Y. Xiao et al., Nat. Rev. Mater. 5 (2020) 105–126.
[19] T. Famprikis et al., Nat. Mater. 18 (2019) 1278–1291.
[20] R.C. Xu et al., Electrochim. Acta 284 (2018) 177–187.
[21] L. Xu et al., Joule 2 (2018) 1991–2015.
[22] C. Monroe, J. Newman, J. Electrochem. Soc. 152 (2005) A396–A404.
[23] D.H.S. Tan et al., Nat. Nanotech. 15 (2020) 170–180.
[24] A.M. Tripathi et al., Chem. Soc. Rev. 47 (2018) 736–851.
[25] D. Liu et al., Adv. Mater. 31 (2019) 1806620.
[26] C. Korepp et al., J. Power Sources 158 (2006) 578–582.
[27] H.J. Santner et al., Anal. Bioanal. Chem. 379 (2004) 266–271.
[28] J. Lu et al., Nat. Energy 2 (2017) 17011.
[29] J.Y. Huang et al., Science 330 (2010) 1515–1520.
[30] X.H. Liu et al., Nano Lett. 11 (2011) 3991–3997.
[31] X.H. Liu et al., Nat. Nanotech. 7 (2012) 749–756.
[32] J.W. Wang et al., Nano Lett. 13 (2013) 709–715.
[33] G. Zheng et al., Nat. Nanotech. 9 (2014) 618–623.
[34] M.T. McDowell et al., Nano Lett. 15 (2015) 1264–1271.
[35] J. Wang et al., Nano Lett. 16 (2016) 5815–5822.
[36] L. Zhong et al., Adv. Mater. 29 (2017) 1700236.
[37] M.G. Boebinger et al., Joule 2 (2018) 1783–1799.
[38] Q.B. Zhang et al., Energy Environ. Sci. 11 (2018) 669–681.
[39] L. Zhao et al., ACS Nano 12 (2018) 12597–12611.
[40] Q. Liu et al., Energy Storage Mater. 19 (2019) 48–55.
[41] J. Li et al., Nat. Commun. 10 (2019) 2224.
[42] W. Zhang et al., Nat. Commun. 10 (2019) 1972.
[43] A.W. Xiao et al., Nat. Mater. 19 (2020) 644–654.
[44] Z. Zheng et al., ACS Nano 14 (2020) 9545–9561.
[45] X.H. Liu et al., Nano Lett. 11 (2011) 3312–3318.
[46] L. Luo et al., Nat. Nanotech. 12 (2017) 535–539.
[47] L. Zhang et al., Nat. Nanotech. 15 (2020) 94–98.
[48] Y. He et al., Nat. Nanotech. 14 (2019) 1042–1047.
[49] D. Ruzmetov et al., Nano Lett. 12 (2012) 505–511.
[50] Z. Wang et al., Nano Lett. 16 (2016) 3760–3767.
[51] M. Kuhne et al., Nature 564 (2018) 234–239.
[52] H. Xu et al., Mater. Today Nano 7 (2019) 100042.
[53] Y.F. Yuan et al., Nat. Commun. 8 (2017) 15806.
[54] Z. Fan et al., Adv. Mater. 31 (2019) 1900608.
[55] J. Li et al., Joule 3 (2019) 4–8.
[56] Q. Gao et al., Chem. Mater. 26 (2014) 1660–1669.
[57] Y. Yuan et al., Nat. Commun. 8 (2017) 1–14.
[58] X.H. Liu et al., Adv. Energy Mater. 2 (2012) 722–741.
[59] M. Gu et al., Nano Lett. 13 (2013) 6106–6112.
[60] S.W. Lee et al., Nano Lett. 11 (2011) 3034–3039.
[61] J.L. Goldman et al., Adv. Funct. Mater. 21 (2011) 2412–2422.
[62] X.H. Liu, J.Y. Huang, Energy Environ. Sci. 4 (2011) 3844–3860.
[63] R.J. Zou et al., J. Mater. Chem. A 5 (2017) 20072–20094.
[64] Y.T. Wu, N.A. Liu, Chem 4 (2018) 438–465.
[65] X. Liu, L. Gu, Small Methods 2 (2018) 1800006.
[66] J. Woods et al., Nano Energy 56 (2019) 619–640.
[67] C.M. Wang, J. Mater. Res. 30 (2015) 326–339.
[68] T.T. Shang et al., Adv. Energy Mater. 7 (2017) 1700709.
[69] X. Wu et al., Electrochem. Energy Rev. 2 (2019) 467–491.
[70] M.S. Whittingham, Chem. Rev. 104 (2004) 4271–4301.
[71] B.L. Ellis et al., Chem. Mater. 22 (2010) 691–714.
[72] A. Manthiram et al., Chem. Rev. 114 (2014) 11751–11787.
[73] A. Eftekhari, Sustainable Energy Fuels 1 (2017) 14–29.
[74] G.G. Amatucci, N. Pereira, J. Fluorine Chem. 128 (2007) 243–262.
[75] X. Li et al., Nano Energy 42 (2017) 122–128.
[76] T. Placke et al., J. Solid State Electrochem. 21 (2017) 1939–1964.
[77] J. Lu et al., Chem. Rev. 114 (2014) 5611–5640.
[78] K. Mizushima et al., Mater. Res. Bull. 15 (1980) 783–789.
[79] J.N. Reimers, J.R. Dahn, J. Electrochem. Soc. 139 (1992) 2091–2097.
[80] G.G. Amatucci et al., J. Electrochem. Soc. 143 (1996) 1114–1123.
[81] J. Cho et al., J. Electrochem. Soc. 148 (2001) A1110–A1115.
[82] S. Krueger et al., J. Electrochem. Soc. 160 (2013) A542–A548.
[83] Y. Gong et al., J. Am. Chem. Soc. 139 (2017) 4274–4277.
[84] H. Wang et al., J. Electrochem. Soc. 146 (1999) 473–480.
[85] Z. Yang et al., Small 14 (2018) e1803108.
[86] N. Nitta et al., Mater. Today 18 (2015) 252–264.
[87] A. Manthiram et al., Adv. Energy Mater. 6 (2016) 1501010.
[88] Y. Nomura et al., ACS Energy Lett. 5 (2020) 2098–2105.
[89] M.M. Thackeray et al., Mater. Res. Bull. 19 (1984) 179–187.
[90] D.K. Kim et al., Nano Lett. 8 (2008) 3948–3952.
[91] S. Lee et al., ACS Nano 9 (2015) 626–632.
[92] R. Santhanam, B. Rambabu, J. Power Sources 195 (2010) 5442–5451.
[93] H. Liu et al., J. Power Sources 300 (2015) 430–437.
[94] J. Ma et al., Chem. Mater. 28 (2016) 3578–3606.
[95] X. Cao et al., ACS Appl. Mater. Interfaces 8 (2016) 25971–25978.
[96] H. Liu et al., ACS Appl. Mater. Interfaces 8 (2016) 4661–4675.
[97] M. Lin et al., Chem. Mater. 27 (2014) 292–303.
[98] B. Chen et al., Chem. Mater. 30 (2018) 2174–2182.
[99] Y. Gong et al., Nat. Commun. 9 (2018) 3341.
[100] P. Kalyani et al., J. Power Sources 80 (1999) 103–106.
[101] H. Yu, H. Zhou, J. Phys. Chem. Lett. 4 (2013) 1268–1280.
[102] J. Zheng et al., Nano Lett. 14 (2014) 2628–2635.
[103] M. Sathiya et al., Nat. Mater. 12 (2013) 827–835.
[104] F. Yang et al., Adv. Funct. Mater. 29 (2019) 1808291.
[105] J. Rana et al., J. Electrochem. Soc. 163 (2016) A811–A820.
[106] J. Wang et al., Adv. Energy Mater. 6 (2016) 1600906.
[107] X. He et al., J. Mater. Chem. A 4 (2016) 7230–7237.
[108] A.D. Robertson, P.G. Bruce, Chem. Mater. 15 (2003) 1984–1992.
[109] R. Wang et al., Adv. Energy Mater. 3 (2013) 1358–1367.
[110] P.F. Yan et al., Chem. Mater. 27 (2015) 975–982.
[111] D. Mohanty et al., Chem. Mater. 26 (2014) 6272–6280.
[112] J. Rana et al., Adv. Energy Mater. 4 (2014) 1300998.
[113] Q. Li et al., Nat. Commun. 10 (2019) 1692.
[114] A.K. Padhi et al., J. Electrochem. Soc. 144 (1997) 1188–1194.
[115] C. Delacourt et al., J. Electrochem. Soc. 152 (2005) A913–A921.
[116] C. Delmas et al., Nat. Mater. 7 (2008) 665–671.
[117] C.V. Ramana et al., J. Power Sources 187 (2009) 555–564.
[118] L. Gu et al., J. Am. Chem. Soc. 133 (2011) 4661–4663.
[119] R. Malik et al., Nat. Mater. 10 (2011) 587–590.
[120] Y. Zhu et al., Adv. Mater. 25 (2013) 5461–5466.
[121] J. Niu et al., Nano Lett. 14 (2014) 4005–4010.
[122] S. Kobayashi et al., Nano Lett. 16 (2016) 5409–5414.
[123] X. Ji et al., Nat. Mater. 8 (2009) 500–506.
[124] N. Jayaprakash et al., Angew. Chem. Int. Ed. 50 (2011) 5904–5908.

[125] X. Ji, L.F. Nazar, J. Mater. Chem. 20 (2010) 9821–9826.
[126] X. Chen et al., Mater. Today 22 (2019) 142–158.
[127] J. Kim et al., Adv. Funct. Mater. 23 (2013) 1076–1080.
[128] Q. Pang et al., Nat. Energy 1 (2016) 16132.
[129] G. Bieker et al., Phys. Chem. Chem. Phys. 19 (2017) 11152–11162.
[130] M. Liu et al., Nano Energy 22 (2016) 278–289.
[131] J. Lee et al., ACS Energy Lett. 2 (2017) 1232–1239.
[132] J.C. Bachman et al., Chem. Rev. 116 (2016) 140–162.
[133] E. Umeshbabu et al., Electrochem. Energy Rev. 2 (2019) 199–230.
[134] D.N. Lei et al., Adv. Funct. Mater. 28 (2018) 1707570.
[135] R. Xu, et al., ACS Appl. Mater. Interfaces 6 (2014) 21938-21945..
[136] H. Kim et al., Adv. Energy Mater. 5 (2015).
[137] Q. Pang et al., Nat. Commun. 5 (2014) 4759.
[138] W. Tang et al., J. Am. Chem. Soc. 139 (2017) 10133–10141.
[139] A. Abouimrane et al., J. Am. Chem. Soc. 134 (2012) 4505–4508.
[140] Z. Li et al., Nano Energy 9 (2014) 229–236.
[141] C.P. Yang et al., Angew. Chem. Int. Ed. 52 (2013) 8363–8367.
[142] J. Ding et al., Adv. Energy Mater. 8 (2018) 1701918.
[143] X. Li et al., Energy Environ. Sci. 11 (2018) 2828–2832.
[144] X. Li et al., Adv. Mater. 31 (2019) 1808100.
[145] Q. Li et al., ACS Nano 10 (2016) 8788–8795.
[146] Y.H. Li et al., Nano Energy 48 (2018) 441–447.
[147] R.R. Mitchell et al., Energy Environ. Sci. 4 (2011) 2952–2958.
[148] J. Christensen et al., J. Electrochem. Soc. 159 (2012) R1–R30.
[149] J.J. Xu et al., Nat. Commun. 4 (2013) 2438.
[150] Y.Y. Shao et al., Adv. Funct. Mater. 23 (2013) 987–1004.
[151] F. Li et al., Energy Environ. Sci. 6 (2013) 1125–1141.
[152] Z. Liang et al., Small Methods 1 (2017) 1700150.
[153] Y.-C. Lu et al., Energy Environ. Sci. 6 (2013) 750–768.
[154] A. Kushima et al., Nano Lett. 15 (2015) 8260–8265.
[155] L. Johnson et al., Nat. Chem. 6 (2014) 1091.
[156] L. Zhong et al., Nano Lett. 13 (2013) 2209–2214.
[157] X. Huang et al., Chem. Soc. Rev. 42 (2013) 1934–1946.
[158] C. Tan et al., Chem. Rev. 117 (2017) 6225–6331.
[159] M.S. Whittingham, Science 192 (1976) 1126–1127.
[160] X. Zang et al., Adv. Mater. 30 (2018) 1704754.
[161] J.M. Whiteley et al., J. Mater. Chem. A 5 (2017) 15661–15668.
[162] L. Zhang et al., Nano Lett. 18 (2018) 4506–4515.
[163] M.S. Fu et al., Nano Energy 63 (2019) 103882.
[164] M.S. Whittingham, J. Electrochem. Soc. 123 (1976) 315–320.
[165] Z. Lin et al., ACS Nano 7 (2013) 2829–2833.
[166] K. Cai et al., Nano Lett. 12 (2012) 6474–6479.
[167] Z.W. Seh et al., Energy Environ. Sci. 7 (2014) 672–676.
[168] H. Yan et al., Nano Lett. 19 (2019) 3280–3287.
[169] Z. Wei Seh et al., Nat. Commun. 4 (2013) 1331..
[170] W. Li et al., Proc. Natl. Acad. Sci. USA 110 (2013) 7148–7153.
[171] Y. Yang et al., Nano Lett. 10 (2010) 1486–1491.
[172] J. Hassoun, B. Scrosati, Angew. Chem. Int. Ed. 49 (2010) 2371–2374.
[173] G. Tan et al., Nat. Energy 2 (2017) 17090.
[174] F. Wang et al., Nat. Commun. 6 (2015) 6668.
[175] K. Turcheniuk et al., Nature 559 (2018) 467–470.
[176] W. Gu et al., Adv. Energy Mater. 5 (2015) n/a-n/a..
[177] Q. Huang et al., Nat. Mater. 18 (2019) 1343–1349.
[178] F. Wang et al., Nat. Commun. 3 (2012) 1201.
[179] P.L. Taberna et al., Nat. Mater. 5 (2006) 567–573.
[180] F. Badway et al., J. Electrochem. Soc. 150 (2003) A1209–A1218.
[181] F. Wang et al., J. Am. Chem. Soc. 133 (2011) 18828–18836.
[182] F. Badway et al., J. Electrochem. Soc. 150 (2003) A1318–A1327.
[183] K. Karki et al., J. Am. Chem. Soc. 140 (2018) 17915–17922.
[184] X. Fan et al., Nat. Commun. 9 (2018) 2324.
[185] J.M. Tarascon, M. Armand, Nature 414 (2001) 359–367.
[186] W. Xu et al., Energy Environ. Sci. 7 (2014) 513–537.
[187] J. Liu et al., Nat. Energy 4 (2019) 180–186.
[188] Y.Q. Chen et al., Small Methods 3 (2019) 1800551.
[189] Y. Zhang et al., Mater. Today 33 (2020) 56–74.
[190] K. Yan et al., Nat. Energy 1 (2016) 16010.
[191] H. Wang et al., Nano Lett. 19 (2019) 1326–1335.
[192] X.N. Lan et al., Nano Energy 66 (2019) 104178.
[193] D. Lin et al., Nat. Nanotech. 11 (2016) 626–632.
[194] S. Liu et al., Joule 2 (2018) 184–193.
[195] W. Ye et al., Adv. Energy Mater. 10 (2020) 1902956.
[196] Y. Chen et al., Nature 578 (2020) 251–255.
[197] M.-H. Ryou et al., Adv. Funct. Mater. 25 (2015) 834–841.
[198] J. Becking et al., Adv. Mater. Interfaces 4 (2017) 1700166.
[199] P. Schmitz et al., Phys. Chem. Chem. Phys. 19 (2017) 19178–19187.
[200] T. Yang et al., Angew. Chem. Int. Ed. 57 (2018) 12750–12753.
[201] X. Wang et al., Chem. Commun. 48 (2012) 4812–4814.
[202] J. Janek, W.G. Zeier, Nat. Energy 1 (2016) 16141.
[203] Z. Gao et al., Adv. Mater. 30 (2018) 1705702.
[204] L. Fan et al., Adv. Energy Mater. 8 (2018) 1702657.
[205] Y. Wang et al., Nat. Mater. 14 (2015) 1026–1031.
[206] W.D. Richards et al., Chem. Mater. 28 (2016) 266–273.
[207] K. Zhao et al., Adv. Energy Mater. 7 (2017) 1601582.
[208] W. Luo et al., Adv. Mater. 29 (2017) 1606042.
[209] F. Han et al., Joule 2 (2018) 497–508.
[210] X.Z. Chen et al., Energy Environ. Sci. 12 (2019) 938–944.
[211] J. Fu, J. Am. Chem. Soc. 80 (1997) 1901–1903.
[212] K. Yamamoto et al., Angew. Chem. Int. Ed. 49 (2010) 4414–4417.
[213] Y. Nomura et al., Nano Lett. 18 (2018) 5892–5898.
[214] Y. Nomura et al., Nat. Commun. 11 (2020) 2824.
[215] X. Yu et al., J. Electrochem. Soc. 144 (1997) 524–532.
[216] D. Santhanagopalan et al., J. Phys. Chem. Lett. 5 (2014) 298–303.
[217] J.B. Goodenough et al., Mater. Res. Bull. 11 (1976) 203–220.
[218] J.S. Thokchom, B. Kumar, J. Power Sources 185 (2008) 480–485.
[219] M. Zhang et al., J. Electrochem. Soc. 159 (2012) A1114–A1119.
[220] H. Chung, B. Kang, Chem. Mater. 29 (2017) 8611–8619.
[221] J.A. Lewis et al., ACS Energy Lett. 4 (2019) 591–599.
[222] W. Zhou et al., J. Am. Chem. Soc. 138 (2016) 9385–9388.
[223] F. Han et al., Nat. Energy 4 (2019) 187–196.
[224] S.-S. Chi et al., Energy Storage Mater. 17 (2019) 309–316.
[225] Q. Cheng et al., Joule 3 (2019) 1510–1522.
[226] J. Zhu et al., Chem. Mater. 32 (2020) 4998–5008.
[227] V. Thangadurai et al., Chem. Soc. Rev. 43 (2014) 4714–4727.
[228] C. Ma et al., Nano Lett. 16 (2016) 7030–7036.
[229] Y. Li et al., Science 358 (2017) 506–510.
[230] X. Wang et al., Nano Lett. 17 (2017) 7606–7612.
[231] M.J. Zachman et al., Nature 560 (2018) 345–349.
[232] P. Yan et al., Nat. Nanotech. 14 (2019) 602–608.
[233] L. Li et al., Nano Lett. 20 (2020) 2756–2762.
[234] I. Lazić et al., Ultramicroscopy 160 (2016) 265–280.
[235] A. Nie et al., ACS Nano 7 (2013) 6203–6211.
[236] M.J. Zachman et al., Angew. Chem. Int. Ed. 59 (2020) 1384–1396.
[237] S. Ahmed et al., Adv. Energy Mater. 10 (2020) 2001026.